Mmp14-controlled extracellular matrix homeostasis is required for circadian rhythm

Richa Garva[1ψ] , Ching-Yan Chloé Yeung[1ψ], Adam Pickard[1ψ], Yinhui Lu[1], Venkatesh Mallikarjun[1], Joe Swift[1], Susan H. Taylor[1], Jyoti Rai[2], David R. Eyre[2], Mayank Chaturvedi[3], Yoshifumi Itoh[3], Qing-Jun Meng[1], Cornelia Mauch[4], Paola Zigrino[4], and Karl E. Kadler[1]*

[1] Wellcome Centre for Cell-Matrix Research, Faculty of Biology, Medicine & Health, University of Manchester, Manchester Academic Health Science Centre, Manchester, M13 9PT UK

[2] Department of Orthopedics, University of Washington, Seattle, WA, USA

[3] Kennedy Institute of Rheumatology, University of Oxford, Oxford, UK

[4] Department of Dermatology and Venereology, University of Cologne, Faculty of Medicine and University Hospital Cologne, 50937 Cologne, Germany

C-YCY current address: Institute of Sports Medicine Copenhagen, Department of Orthopedic Surgery, Copenhagen University Hospital – Bispebjerg and Frederiksberg, Copenhagen, Denmark, and Center for Healthy Aging, Department of Clinical Medicine, University of Copenhagen, Denmark

[ψ] Equal first authors.

*Corresponding author: K.E.K. (email: karl.kadler@manchester.ac.uk)

Keywords: MT1-MMP; chronomatrix; circadian clock; tendon, actin, focal adhesions

SUMMARY

The circadian clock regulates extracellular matrix (ECM) homeostasis but whether altered ECM homeostasis regulates the clock was unknown. Thus, we generated mice with a Col1a2-Cre-ERT2 conditional deletion of matrix metalloproteinase-14 (*Mmp14*) to disrupt matrix homeostasis in postnatal mice. We show here that tamoxifen-treated Col1a2-Cre-ERT2::Mmp14$^{F/F}$ mice developed a severe tendon matrix phenotype with dorsiflexion of hind limbs, tissue thickening, and accumulation of hydroxylysine aldehyde (pyridinoline) crosslinked narrow-diameter collagen fibrils typically seen accumulating during embryonic development. Proteomic analysis of tamoxifen-treated postnatal mice showed ~16% of detected proteins lost (176 proteins) or reversed (19 proteins) time-dependent rhythmicity. Ontological analysis identified 'cytoskeleton' as an affected system. Subsequent studies in CRISPR-Cas9 *Mmp14* null cells showed decreased F-/G-actin ratio, decreased cell spreading, elevated levels of pyridinoline crosslink factor *Plod2,* nuclear translocation of transcription factor *Pitx2*, and loss of circadian rhythm. Thus, our study shows a bidirectional dependence of collagen-ECM homeostasis and the circadian clock.

INTRODUCTION

MT1-MMP (gene name *Mmp14*) is a transmembrane matrix metalloproteinase first identified for its ability to activate progelatinase A (proMMP2) and to enhance cellular invasion of reconstituted basement membrane [1]. Extensive studies have showed that it can cleave a wide range of cellular and extracellular substrates including protease inhibitors, chemokines, cytokines, cell receptors, proMMP13, fibronectin and collagens (see [2]). Therefore, disrupted *Mmp14* expression has a major disruptive effect on matrix homeostasis. In humans, *Mmp14* has been implicated in cancer cell invasion [3, 4], which has been attributed to its ability to degrade extracellular matrix (ECM) macromolecules, especially type I collagen (collagen-I) [5-7]. Like other vertebrate collagenases, it cleaves fibrillar collagens at the characteristic ¾-¼ site between residues 775 and 776 in each collagen α-chain [8]. MT1-MMP is distinct from other MMPs in that its deletion in mice results in early postnatal death [9, 10]. The mice fail to thrive and exhibit a wide range of pathologies including defective osteogenesis and angiogenesis [9-11], altered white adipose tissue [12] and tendon [13]

development, modulation of inflammatory responses [14], activation of TGFβ1 [15], and regulation of α5β1 integrin endocytosis [16].

We noted that the organ systems affected in the *Mmp14* null mouse overlap with organ systems that are affected in mice that lack a functional circadian clock. Circadian clocks are cell-autonomous time keeping mechanisms that optimize cellular activities in anticipation of varying time-of-day demands on the cell [17, 18]. Whilst the suprachiasmatic nucleus is the master circadian pacemaker, almost all tissues have self-sustaining circadian pacemakers that synchronize rhythmic tissue-specific gene expression in anticipation of environmental light and dark cycles [19, 20]. Of particular interest, bone formation [19], tendon homeostasis [21, 22], adipogenesis [23], inflammatory immune responses [24], and angiogenesis [25] are processes that are regulated by the circadian clock and are affected in *Mmp14*-deficient mice. A search of public databases showed that transcripts for *Mmp14* are under circadian clock control in mouse suprachiasmatic nucleus (SCN), lung, heart, and adipose tissue[26]. Time-series transcriptomic profiling of mouse tendon (ArrayExpress accession no. E-MTAB-7743 [21]) showed circadian expression of the *Mmp14* transcript. However, direct mechanistic support for the importance of *Mmp14* rhythmicity was lacking.

Here we show in mouse tendon that *Mmp14* (RNA) and MT1-MMP (protein) are under robust circadian clock control and that fibroblasts lacking MT1-MMP are arrhythmic. We generated a type I collagen-specific conditional *Mmp14* knockout (CKO) mouse (*Col1a2*^{CreERT2}*::Mmp14*$^{F/F}$). Loss of circadian rhythm in the mice resulted in a severe tendon phenotype manifested as tissue thickening and dysregulation of cytoskeletal and matrisome proteins. Embryonic tendon contains exclusively 50-nm diameter collagen fibrils attached to cells via fibripositors. At birth, the fibrils are released from cells and grow in diameter to generate a multimodal diameter distribution, which is a developmental process that requires *Mmp14* [13]. Adult tendon contains a small population of narrow collagen fibrils (D1, ~50 nm diameter) that are under circadian clock control [22]. We show here that D1 fibrils accumulate in *Mmp14* CKO tendons. We also showed that recombinant MT1-MMP was effective at cleaving soluble collagen but not fibrillar collagen; thus the accumulation of collagen fibrils in the absence of MT1-MMP was the result of elevated fibrillogenesis and not the lack of turnover of collagen fibrils. One of the major changes in *Mmp14* null tendon was upregulation of proteins whose expression is controlled by the transcription factor *Pitx2* as well as *Plod2, Plod3,* and *LOX* that render the collagen network insoluble. We subsequently showed that collagen in *Mmp14* null tendons is stabilized by hydroxylysine aldehyde (pyridinoline) crosslinks. Therefore, the complex phenotype and progressive tissue fibrosis in *Mmp14*-deficient mice is most likely the consequence of disruption of circadian rhythm, loss of cytoskeleton in fibroblasts, accumulation of proteins that would normally be substrates for MT1-MMP, and constitutive expression of the lysyl hydroxylase/lysyl oxidase crosslinking program to generate insoluble collagen fibrils.

RESULTS

Mmp14 (RNA) and MT1-MMP (protein) show circadian rhythms in expression in tendon

The expression of *Mmp14*, but not other MMPs, is 24-hour rhythmic in tendon [21]. The readouts from 3 independent microarray probe sets showed the highest expression of *Mmp14* at the night-day transition (**Figure 1a**). Time-series western blot analysis showed peak levels of MT1-MMP at CT3 (**Figure 1b**), 4 hours after the peak in transcript. Next, we showed that time-of-day dependent expression of *Mmp14* (in mouse Achilles and tail tendon) was abolished in Scx-Cre::Bmal1$^{F/F}$ and CLOCKΔ19 mice (**Figure 1c-e**), which lack circadian rhythms in their tendons [22]. As such, the rhythmic expression of *Mmp14* depends on an intact local circadian clock in tendon tissues.

We isolated tail tendon fibroblasts from the PER2::Luc mouse (iTTF-PER2::Luc or abbreviated to 'iTTF'), which enabled us to monitor the circadian clock in cultured cells using bioluminescence analysis using previously described methods [22]. In initial experiments we performed siRNA knockdown of *Mmp14.* Q-PCR showed that

knockdown was highly effective at reducing the expression of *Mmp14* (**Extended data figure 1a**) and bioluminescence showed that the circadian clock rhythm was dampened in si-Mmp14 treated cells (**Extended data figure 1b**). In a separate experiment, we incubated iTTF cells with GM6001 (a broad spectrum MMP inhibitor) (**Extended data figure 1c)**, which was also highly effective at dampening circadian rhythm in treated cells compared to untreated controls (**Extended data figure 1d**). Next, we performed clustered regularly interspaced short palindromic repeats (CRISPR)-associated protein 9 (Cas9) mediated knockout of *Mmp14* in PER2::Luc fibroblasts (**Figure 1f, g**). Western blot analysis using an anti-MT1-MMP antibody showed absence of MT1-MMP in 7 different clones (**Figure 1h**). Clones 1 and 2 were unable to sustain a circadian rhythm in response to dexamethasone (**Figure 1i**), forskolin or 50% serum (**Extended data figure 1e, f**), compared to matched cells, and restoring Mmp14 levels by lentiviral transduction rescued this defect enabling robust oscillations (**Figure 1j**).

Accumulation of narrow collagen fibrils in tendons of the *Mmp14* conditional knockout mouse

Because global knockout of *Mmp14* results in perinatal death, we generated the tamoxifen-inducible collagen-I-specific *Mmp14* knockout mouse (*Col1a2*^{CreERT2}*::Mmp14*$^{F/F}$) [27] to study the consequences of postnatal *Mmp14* KO on the circadian clock. Thus, we treated five-week-old *Col1a2*^{CreERT2}*::Mmp14*$^{F/F}$ mice with tamoxifen for 4 weeks and collected mice at 10-, 14-, 18- and 23-week of age (see schematic in **Figure 2a**). We noticed that tamoxifen-treated mice had severe dorsiflexion of the hind limbs and difficulties walking (**Figure 2b**). Therefore, under Home Office guidance, only small numbers of mice were available for study. Examination of the limbs showed thickening of tendon bundles (**Figure 2c**). Transmission EM analysis showed a progressive increase in the abundance of D1 (~ 50 nm diameter) collagen fibrils during T0 to T4 in mice treated with tamoxifen compared to wild-type littermates (**Figure 2d, e** and **Extended data figure 2**). We also noted a gradual increase in irregular fibril profiles from T0 to T4 (**Figure 2f**). Serial block face-scanning electron microscopy, using established methods [28], showed gross disruption of the collagen fibril network and accumulation of narrow fibrils in CKO tendons compared to tendons of littermates not treated with tamoxifen (**Figure 2g, Movie 1** and **Movie 2**).

Recombinant MT1-MMP more effective at cleaving soluble collagen-I than fibrillar collagen-I

The accumulation of D1 collagen fibrils in the CKO tendons could have been explained by the absence of fibril turnover in the absence of MT1-MMP. To explore this possibility, we released collagen fibrils from 6-week-old mouse Achilles tendon and examined the diameters after incubation with recombinant soluble Fc-fusion MT1-MMP *in vitro* [29]. The fibril diameters were derived from mass per length measurements using scanning transmission electron microscopy [30]. The results showed no differences between rMT1-MMP treated and untreated samples (**Figure 3a**). We then incubated the suspension of fibrils and soluble collagen-I with rMT1-MMP at 30 °C and 37 °C. Gel electrophoresis confirmed efficient cleavage of soluble collagen-I by rMT1-MMP at 30 °C, which was inhibited by EDTA (**Figure 3b**, red box). Liquid chromatography with tandem mass spectrometry (LC-MS/MS) analysis of the cleavage products showed the presence of a semi-tryptic peptide from the ¾ α1(I) fragment corresponding to the expected ¾-¼ cleave site, which confirmed that rMT1-MMP had cleaved soluble collagen-I molecules at the expected Gly775 and Ile776 site (**Figure 3c** and **d**). However, the results obtained when the suspension of fibrils was incubated with rMT1-MMP were different from those obtained with soluble collagen-I. Here, only a small proportion of the collagen was cleaved when the reaction was carried out at 30 °C (**Figure 3b**, white box); as expected, the cleavage was inhibited by EDTA. When the reaction was carried out at 37 °C, no cleavage of collagen α-chains was observed. We did notice a downward shift in mobility of β-chains (crosslinked α-chains), which was not inhibited by EDTA. It is likely that this was the result of non-MMP activity in the collagen fibril preparation (**Figure 3b**). We noted that rMT1-MMP cleaved a small proportion of the collagen-I from the fibril suspension when the reaction was performed at 30 °C. The most likely explanation was partial depolymerization of the fibrils at this temperature, resulting

132 in release of collagen molecules that were then susceptible to cleavage by rMT1-MMP. These results showed
133 that collagen is largely protected from cleavage by rMT1-MMP when the collagen is assembled into fibrils.

134 Tendons of the *Col1a2*^{CreERT2}*:Mmp14*$^{F/F}$ null mice lose time-dependent features

135 Next, using mice kept in 12-hr light/12-hr dark conditions, we performed proteomics analysis of tendon
136 harvested at two time points during 24 h (zeitgeber time, ZT) ZT3 (09:00-hrs; 3 hours into light) and ZT15
137 (21:00; 3 hours into dark) from CKO *Mmp14* mice (n = 3) and control littermates (n = 3) at T2 (14 weeks of
138 age; 5 weeks after tamoxifen induction) (see schematic, **Figure 4a**). T2 (5 weeks post tamoxifen treatment)
139 was chosen because there were sufficient numbers of healthy mice in the control and CKO groups (whilst
140 allowing other mice to age to T4 for the electron microscopy study) and T2 was the time where a more
141 prominent fibrotic phenotype was detected in skin and tendons and deletion of *Mmp14* was complete [27]. We
142 extracted proteins using methods previously described [22]. Analysis of samples isolated at ZT3 and ZT15
143 identified 1195 proteins with ≥ 2 peptides per protein of which 212 showed time-dependent abundance, as
144 shown by MetaCycle analysis (**Figure 4a**), with good reproducibility between biological replicates as indicated
145 by Pearson analysis across consecutive 24-hour periods (**Extended data figure 3a**). Comparing logged
146 ZT15/ZT3 fold changes for 1195 proteins between CKO and wild-type tendons showed that the absence of
147 *Mmp14* disrupted time-dependent protein abundances (**Extended data figure 3b**). Of the time-dependent
148 proteins detected in WT tendons, 17 have a statistically significant (FDR adjusted p-value <0.05) difference
149 in expression between the MMP14KO_CT3 and MMP14KO_CT15 but remained time-dependent, 19 had
150 reversed time-dependence (**Figure 4b**), and 176 had lost time-dependent expression in CKO tissues (**Figure
151 4c**). Functional annotation enrichment of the proteomic data using DAVID [31] showed that the proteins that
152 had remained time dependent were predominantly involved in intermediate filament assembly, metabolism,
153 cell-matrix adhesion and microtubule transport (**Figure 4d**). Those that had flipped time dependence (i.e.
154 those normally expressed at night and were expressed in the day in KO cells, and vice versa) and those that
155 had lost time-dependent expression were associated with actin cytoskeleton remodeling (**Figure 4e**) and
156 extracellular matrix including fibronectin, members of the small proteoglycan family, and enzymes involved
157 in collagen crosslinking. (**Supplementary data 1**).

158 *CRISPR/Cas9 knockout of Mmp14* knocks out the circadian rhythm and disrupts F-actin

159 In the next series of experiments, we used CRISPR-Cas9 to knockout *Mmp14* transcripts in fibroblasts and in
160 MC3T3 osteoblasts (which also express *Mmp14*) and performed cell adhesion assays. The first observation
161 was that *Mmp14* KO fibroblasts and osteoblasts were defective at spreading on fibronectin compared to
162 control (**Figure 5a-c**). Secondly, the number (but not the size) of focal adhesions per cell was reduced in
163 *Mmp14* KD fibroblasts (**Figure 5d, e**). Thirdly, staining with phalloidin and immunofluorescence using an anti-
164 vinculin antibody showed absence of an F-actin cytoskeleton in the *Mmp14* KO cells (**Figure 5f**). Western
165 blot analysis showed that the CKO cells had a decreased F-/G-actin ratio (**Figure 5g**), which was consistent
166 with the ontological analysis performed on the proteomics datasets (**Figure 4e**).

167 Circadian actin dynamics have been shown to drive rhythmic fibroblast mobilization during wound healing
168 [32], therefore we incubated fibroblasts with cytochalasin B and measured the circadian rhythm by
169 bioluminescence. The results show that disruption of the cytoskeleton dampened, but did not eradicate, the
170 circadian rhythm in tendon fibroblasts (**Figure 6a**). The organization of focal adhesions is complex and
171 involves cytoskeletal proteins such as vinculin and protein tyrosine kinases such as FAK (see [33]). We showed
172 that shRNA knockdown of vinculin dampened but did not stop the circadian rhythm (**Figure 6b, Extended
173 data figure 1g-h**). Furthermore, treatment with the FAK inhibitor had a pronounced effect on the amplitude
174 of the bioluminescence signal in the iTTFs and was able to rescue the circadian rhythm in *Mmp14* knockout
175 cells (**Figure 6c-e**).

176 Elevated collagen crosslinking in the absence of *Mmp14*

177 There was clear discrepancy between the increased tendon thickening and increased collagen fibril number
178 in the CKO mice (see **Figure 2**) compared to the low levels of collagen-I detected in the time-dependent
179 proteomics of CKO tissues (**Supplementary data 1**). Therefore, we collected tendons from T2 wild-type and
180 CKO mice at ZT3 and ZT15 and performed hydroxyproline analysis on whole tendons. We also subjected
181 tendons to extraction in SL-DOC (sodium laurate-sodium deoxycholate) buffer to isolate soluble proteins
182 followed by hydroxyproline quantification. As shown in **Table 1**, analysis of whole tendons showed that CKO
183 samples contained a higher content of collagen (as measured by hydroxyproline) than WT samples, which
184 was consistent with the increased tendon thickening and increased numbers of collagen fibrils in the CKO
185 mice. However, the amount of hydroxyproline in the SL-DOC samples showed less collagen in the CKO
186 samples than in the WT controls. We then subjected CKO and control samples to cross-linking analyses. The
187 results showed ~ 8-fold increase in hydroxylysine aldehyde (pyridinoline) in the CKO tendons compared to
188 control tendons. Mass spectrometry ruled out significant amounts of collagen-III as the source of pyridinoline
189 in the CKO samples. Therefore, the discrepancy in the number of collagen-I peptides extracted into SL-DOC
190 buffer, and the marked accumulation of collagen fibrils in the CKO tendons, was the result of decreased
191 extractability caused by increased hydroxylysine aldehyde cross-linking of collagen-I [34] in the CKO tissues. In
192 further experiments we cultured WT and CRISPR-Cas9 *Mmp14* knockout fibroblasts and determined
193 hydroxyproline and hydroxylysine aldehyde crosslink content, as above. The results showed an increase in
194 collagen and hydroxylysine aldehyde crosslink content in *Mmp14* KO cultures (**Table 2**).

195 **Dysregulation of the matrisome in the absence of *Mmp14***

196 Comparison of over-represented proteins in the CKO tendons showed a preponderance of proteins
197 characteristic of fibrous tissues (see **Supplementary Data 1** and selected plots in **Extended data figure 4**).
198 These included fibronectin (up 6-fold), tenascin C (up 4-fold), COL5A1 (up 10-fold), and TIMP2 (3-fold
199 increase). Of particular interest, enzymes that catalyze posttranslational modifications in collagen leading to
200 crosslink formation were also elevated, and included PLOD2 (up 13-fold), and LOXL1 (up 20-fold). Also,
201 decorin and fibromodulin were decreased (~ 2-fold) whilst lumican was increased (~ 2-fold). These small
202 proteoglycans are regulators of collagen fibrillogenesis [35] and C-telopeptide cross-linking of collagen in
203 tendon [36]. Inflammasome markers, including NOD-like receptor family proteins, were either not detected or
204 unchanged.

205 **Elevated Pitx2 and PITX2 nuclear localization in *Mmp14* knockout cells**

206 Analysis of gene ontology terms associated with differentially expressed proteins in the CKO tendons showed
207 that PLOD1, 2, 3 and TPT1 are associated with the transcription factor *Pitx2*. The increased pyridinoline
208 crosslinking in the CKO tendons and the over-representation of the lysyl hydroxylases motivated a study of
209 *Pitx2*, which has been reported to regulate PLOD2 [37, 38], as well as expression of collagen I and V [39]. Firstly,
210 RT-qPCR showed that levels of *Pitx2* mRNA are low in murine tail tendon at both ZT3 and ZT15 but were
211 markedly elevated in the CKO tendons 5 weeks post tamoxifen treatment (**Figure 7a)**. Likewise, PLOD2 levels
212 were low in WT tendon but markedly elevated in the CKO tendons (**Figure 7b**). To facilitate further studies,
213 we expressed PITX2-GFP in iTTFs. Over-expression of PITX2-GFP was confirmed by RT-qPCR (**Figure 7c**) and
214 resulted in a 2-fold increase in expression of *Plod2* (**Figure 7d**). PITX2-GFP localized to cell nuclei but also
215 occurred in the cell body (**Figure 7e,** left column). The translocation of PITX2 to the nucleus has been
216 reported to be influenced by mechanosensors and reactive oxygen species [40]. Co-expression of mCherry-
217 MT1-MMP and PITX2-GFP showed that MT1-MMP and PITX2 localize to distinct puncta in the cell body
218 (**Figure 7e,** second column). However, in CRISPR-Cas9 KO *Mmp14* cells, PITX2-GFP was predominantly in the
219 nucleus (**Figure 7e,** third column). In a rescue experiment, we over-expressed mCherry-MT1-MMP in PITX2-
220 GFP expressing cells in which *Mmp14* was either CRISPR-Cas9 knocked out or not (**Figure 7e**, right hand
221 column). The rescue *Mmp14* carried a silent mutation (AGG to AAA) in the PAM site which did not alter the

222 amino acid sequence of MT1-MMP. The results show that nuclear localization of PITX2-GFP is evident in cells
223 that have not been rescued by mCherry-MT1-MMP.

224 Over-expression of mCherry-MT1-MMP (**Figure 7f**) suppressed both *Pitx2* and *Plod2* expression (**Figure 7g,h**,
225 whilst also resulting in a marked upregulation of *Col1a1* (**Figure 7i**). These results were in-line with a direct
226 relationship between *Pitx2* and *Plod2* as previously reported and the inverse relationship between *Pitx2* and
227 *Mmp14* in the CKO tendons, compared to control. The relationship between *Mmp14* and *Pitx2* in terms of
228 expression levels and cell localization prompted us to determine if Pitx2 levels could impact on circadian
229 rhythm. As shown in **Figure 8**, constitutive expression of PITX2 or PITX2-GFP increased the bioluminescence
230 amplitude in Per2::Luc iTTF cells.

231 **DISCUSSION**

232 In this study we showed that *Mmp14* is under robust circadian clock control and its absence, either by
233 conditional deletion in mice or CRISPR-Cas9 gene editing of cultured cells, causes major matrisome disruption
234 and loss of circadian rhythm. In mice, the consequence was a severe tendon phenotype marked by
235 dorsiflexion of hind limbs, tissue thickening and mistiming and altered levels of 195 proteins. Previous studies
236 showing that the matrix is under circadian clock control and that disruption of the circadian clock leads to
237 tissue fibrosis, and, the results shown here that disruption of the matrix (by deletion of *Mmp14*) results in
238 loss of time-dependent protein expression, identifies a bi-directional dependence of matrix homeostasis and
239 the circadian clock.

240 Circadian clocks are maintained at the molecular level by BMAL1, CLOCK, CRYs and PERs, which are core
241 elements of a transcriptional/translational negative feedback loop that controls the rhythmic expression of
242 genes in a cell-specific manner [41]. Circadian clock responsive genes contain one or more transcriptional
243 elements, RORE, DBPE and E-box [42]. Noteworthy, a CACGTT (E-box) sequence is located 1.6 kb upstream of
244 the translational start site of murine and human *Mmp14. Mmp14* gene expression has been shown to be
245 rhythmically expressed in murine lung, heart, kidney and adipose as well as the suprachiasmatic nucleus [43].
246 These studies showed that limiting the expression of *Mmp14* to a specific time of day is likely to be conserved
247 across species and is likely coincident with *Bmal1* expression. We showed that the peak of *Mmp14*
248 expression in murine tendon is at CT23, which is in good agreement with the peak of *Bmal1* expression [21].
249 Therefore, it is likely that *Mmp14* is a Bmal1 responsive gene. The peak of expression of MT1-MMP was
250 particularly narrow (~ 4 hours after the peak of *Mmp14*) (**Figure 1**), which is consistent with observations
251 that MT1-MMP has a fast turnover of 4.8 hours, which puts it in the top 1% of rapidly turned-over proteins
252 in the proteome [44, 45].

253 Loss of *Mmp14* and circadian rhythmicity in the CKO cells affected ~ 16% of soluble proteins including
254 intracellular and soluble ECM proteins (**Figure 4**). The actin cytoskeleton and F-/G-actin ratio was disrupted
255 in the absence of *Mmp14*, and cells were less able to spread on a fibronectin matrix *in vitro*. In the absence
256 of *Mmp14 in vivo*, circadian clock-controlled D1 fibrils accumulate (**Figure 2**) leading to major disruption of
257 the ECM. Of note, accumulation of D1 fibrils also occurs in clockless fibroblasts [22]. The loss of circadian clock
258 rhythmicity in the absence of *Mmp14* could partially be explained by the depolymerization of the
259 cytoskeleton. However, cytochalasin-D (which binds cofilin [46] and disrupts the F/G-actin dynamics under
260 normal clock control [32]) and removal of vinculin only dampened the rhythm (**Figure 6**). Therefore, we propose
261 that the altered matrisome containing large numbers of crosslinked collagen fibrils, decreased decorin,
262 decreased fibromodulin, and elevated lumican, contribute to the loss of circadian rhythm in *Mmp14* deficient
263 cells.

264 A previous study showed that levels of soluble collagen and the formation of D1 collagen fibrils in healthy
265 murine tendon are under circadian clock control [22]. The peak of soluble collagen occurs in the early part of
266 the day (light cycle), which was attributed to the circadian regulation of the secretory pathway and the

267 rhythmic synthesis and removal of a sacrificial pool of collagen to maintain tissue health. MT1-MMP is a
268 potent collagenase and, as we show, is under strict circadian control. Therefore, if MT1-MMP had a role in
269 degrading collagen fibrils, its expression might be expected to peak at the day/night transition when fibril
270 numbers decrease. However, as shown in **Figure 1**, both *Mmp14* and MT1-MMP peak at the night/day
271 transition, which coincides with when collagen fibrils are assembling. This suggests a role for MT1-MMP in
272 regulating the availability of soluble collagen for fibril assembly. This conclusion is supported by the finding
273 shown in **Figure 3** that MT1-MMP is more effective in cleaving soluble collagen than fibrillar collagen. In
274 further support of this conclusion, mapping functional domains of collagen-I onto the proposed structure of
275 a collagen-I-containing fibril suggests that the fibril surface partially obscures accessibility of MMPs to the
276 775-776 cleavage site [47].

277 Hydroxyproline analysis showed a higher content of collagen in CKO compared to WT samples, which was
278 consistent with the observed accumulation of D1 collagen fibrils in CKO tendons. However, the amount of
279 collagen in the SL-DOC protein extracts was lower in the CKO than in WT. The discrepancy was the result of
280 elevated hydroxylysine aldehyde crosslinking in the CKO tendons that prevented collagen-I from being
281 extracted into SL-DOC buffer. To seek an explanation for elevated crosslinking in the CKO samples, we noted
282 in the LC-MS/MS data elevated PLOD2, PLOD3 and LOX enzymes. Furthermore, there was a 50-fold increase
283 in mRNA levels of *Pitx2* in CKO samples compared to control (**Figure 7**). Previous studies had shown that
284 PITX2 regulates PLOD gene expression [37, 38]. Therefore, a possible explanation for the increased crosslinking
285 in CKO samples was abnormally high activity of PITX2 in the absence to *Mmp14*. Fluorescent tagging of PITX2
286 and MT1-MMP followed by fluorescence microscopy analysis showed that MT1-MMP regulates the
287 intracellular localization of PITX2 protein; in the absence of MT1-MMP, PITX2 is constitutively nuclear
288 located, which according to previous studies would upregulate PLOD2 and the pyridinoline crosslink program.
289 The overall outcome was the accumulation of crosslinked collagen chains in insoluble collagen fibrils.

290 We noticed high peptide counts in the mass spectrometry data for fibronectin, MMP2 and stromelysin 1, 2
291 and 3 in CKO compared to WT littermates. MMP3 and 10 can cleave a range of structural matrix proteins
292 including collagens, proteoglycans, fibronectin and laminin whilst MMP11 cleaves α1-antitrypsin inhibitor
293 and weakly degrades matrix proteins including collagen-IV [48]. MMPs can be activated intracellularly or
294 extracellularly by proteolytic removal of a pro-domain by serine proteinases (e.g. furin[49]). Therefore, whilst
295 these MMPs were elevated in the absence of *Mmp14*, it is possible that they existed in an inactive form.
296 However, removal of the prodomain is not the only mechanism of activation; proMMPs can be activated by
297 conformational changes induced either chemically [50] or by post-translational modifications of the cysteine
298 switch [51]. MMPs can also have intracellular substrates and can reenter the cell (e.g. MT1-MMP [52]), be
299 inefficiently secreted, or have organelle localization signals (reviewed by [53]). Therefore, the changes in the
300 intracellular proteome that we detected by LC-MS/MS might also be expected to affect intracellular
301 processes. Whilst fibronectin and collagen levels were elevated in the absence of MT1-MMP, the levels of
302 small proteoglycans such as decorin, fibromodulin keratocan, and lubricin decreased (**Supplementary data**
303 **1**). The notable exception was lumican, which was elevated ~2-fold in CKO tendons. Lumican is a collagen-
304 binding proteoglycan [54] and was proposed to facilitate interchain collagen crosslinking by interacting with
305 collagen and lysyl oxidase (reviewed by [55]). Lumican has a critical role in the organization of collagen fibrils
306 in tendons and cornea and is profibrotic in heart [56]. Furthermore, lumican knockout leads to reduced collagen
307 crosslinking [57]. Therefore, elevated levels of lumican in the absence of *Mmp14* might also contribute to
308 altered matrix homeostasis and elevated collagen crosslinks in the CKO mice.

309 In conclusion, the inter-dependence between the circadian clock and matrix homeostasis, especially collagen
310 homeostasis, is regulated by the transmembrane metalloproteinase *Mmp14*/MT1-MMP. Lack of collagen
311 homeostasis is a hallmark of fibrosis, which is associated with 45% of all deaths including those caused by

312 cancer [58]. Thus, we propose that targeting the 'circadian clock-matrix homeostasis axis' may provide
313 opportunities for the treatment of fibrosis.

314 **Acknowledgements**
315 The research was funded by Wellcome (110126/Z/15/Z and 203128/Z/16/Z) and the BBSRC (BB/T001984/1)
316 to KEK. CM and PZ were supported by Deutsche Forschungsgemeinschaft through SFB 829 (Project-ID
317 73111208-SFB829 (B4)). VM was supported by a studentship from the Sir Richard Stapley Educational Trust.
318 JS was funded by a Biotechnology and Biological Sciences Research Council (BBSRC) David Phillips Fellowship
319 (BB/L024551/1). BC is supported by a Wellcome PhD studentship (210062/Z/17/Z). MC and YI was funded by
320 Polish Ministry of Science & Higher Education (1291/MOB/IV/2015/0). Q-JM was supported by Medical
321 Research Council project grants MR/T016744/1 and MR/P010709/1 and Versus Arthritis Senior Research
322 Fellowship Award 20875. National Institutes of Health (NIH) Grant: (NIAMS) AR037318 to DRE. The authors
323 would like to thank Ronen Schweitzer (Shriners Hospital for Children, Portland, OR, USA) for *Scx-Cre* mice,
324 Jan Zamek, Alison Hallworth and Raymond Hodgkiss, and the University of Manchester Biological Support
325 Facility for assistance in animal welfare and husbandry. The proteomics was performed at the Biological Mass
326 Spectrometry Facility in the Faculty of Biology, Medicine and Health (University of Manchester) with the
327 assistance of Stacey Warwood and Ronan O'Cualain, and electron microscopy was performed in the Electron
328 Microscopy Facility, Faculty of Biology, Medicine and Health (University of Manchester).

329 **Author contributions:**
330 Conceived the project and provided mechanistic insight: AP, C-YCY, KEK, RG.
331 Interpretation of results regarding the circadian clock: Q-JM.
332 Wrote the manuscript: AP, C-YCY, KEK, RG.
333 Designed experiments and interpreted data: AP, C-YCY, DE, JR, MC, PZ, RG, ST.
334 Provided reagents: CM, PZ, YI.
335 Performed the electron microscopy: YL.
336 Performed bioinformatics analysis: JS, VM.

337 **Competing Interests:**
338 The authors declare no competing interests.

339

340 **Table 1: Collagen content in wild type and CKO tendons determined by hydroxyproline assay.**

	Control		CKO	
	ZT3	ZT15	ZT3	ZT15
Hydroxyproline content of whole tissue (%)	70.97 ± 4.27	62.30 ± 5.25	71.43 ± 1.74	70.40 ± 6.35
Hydroxyproline content of SL-DOC extract (%)	1.50 ± 0.10	0.98 ± 0.31*	1.39 ± 0.12	0.81 ± 0.05*
Hydroxylysine aldehyde (pyridinoline) content (residue/residue hydroxyproline)	0.009 ± 0.003	0.090 ± 0.033	0.095 ± 0.033**	0.095 ± 0.007**

341 Two-way ANOVA: *p=0.0146 for time difference (total collagen), **p=0.0014 for genotype difference.

342

343 **Table 2: Comparison of hydroxyproline and hydroxylysine aldehyde-pyridinoline content in wild type and**
344 ***Mmp14* KO fibroblasts.**

Sample	lyophilized wt (in mg)	Total collagen	% collagen	HP
				res/collagen
WT1	2.09	1.609	77.0	0.0055
WT2	2.07	1.298	62.7	0.0141
WT3	2.18	1.597	73.2	0.0084
WT4	1.17	0.760	65.0	0.0168
WT5	1.13	0.590	52.2	0.0102
WT6	2.3	1.605	69.8	0.0108
			66.6	**0.0110**
KO1	1.75	1.256	71.8	0.0234
KO2	1.89	1.290	68.3	0.1249
KO3	2.19	1.626	74.3	0.1205
KO4	1.09	0.900	82.6	0.1046
KO5	1.06	0.715	67.5	0.1002
KO6	1.32	0.807	61.2	0.0805
			70.9	**0.0923**

345

346

347 **FIGURE LEGENDS**

348 **Figure 1. *Mmp14* expression and MT1-MMP translation in tendon are under circadian clock control.**
349 **A**, Expression of *Mmp14* mRNA in mouse tail tendons analysed by microarray every 4 h during 48 h, relative
350 to the first time point. Three coloured lines indicate the results from 3 probe sets on the microarray chip,
351 n=2; CT, circadian time (free-running time, in constant darkness). **B**, Expression of MT1-MMP in mouse tail
352 tendons analysed by western blotting. Levels of GAPDH protein served as a loading control. **C**, Time-
353 dependent expression of *Mmp14*, measured at zeitgeber time 3 (ZT3; 3 hours into the light phase) and ZT15
354 in mouse Achilles and tail tendons of wild type mice and **D**, tendon-specific *Bmal1* knockout (*Scx-*
355 *Cre::Bmal1*$^{lox/lox}$) mice, n=3; bars show SEM; **p=0.0043 for WT Achilles tendon, **p=0.0093 for WT tail
356 tendon, unpaired t-tests. **E**, relative Mmp14 expression in wild-type and CLOCKΔ19 Achilles and tail tendons,
357 n=3; **F**, Sanger sequencing of *Mmp14* in immortalised tail tendon fibroblasts (iTTFs) derived from the
358 Per2::Luc mouse (iTTFs, upper) and a single cell clone with *Mmp14* CRISPR-Cas9 knockout. Sequences
359 proximal to the gRNA binding site are shown. **G**, Western blot detection in control Per2::luc iTTFs and single
360 cell clones of MMP14 CRISPR-Cas9 knockouts. **H**, bioluminescence recordings from Per2::Luc iTTFs (black)
361 and single cell clones of CRISPR-Cas9 induced knockout of *Mmp14* Per2::Luc fibroblasts (blue) after
362 synchronisation with dexamethasone. **I,** bioluminescence recordings from Per2::Luc iTTFs (grey) or *Mmp14*
363 KO fibroblasts (blue) that have been transduced with a lentivirus expressing *Mmp14* (carrying a silent
364 mutation in the CRISPR-Cas9 PAM site) from a CMV promoter (black and red). Restoration of *Mmp14* levels
365 in *Mmp14* KO fibroblasts reinstated dexamethasone induced circadian rhythms (n=2 independent repeats
366 are shown, error bar represents standard deviation, and represent data from n=4 independent experiments.
367 **J**). Quantification of Per2::Luc amplitudes assessed over 3 days post dexamethasone treatment (n=4).

368 **Figure 2. Accumulation of collagen fibrils in tendons from tamoxifen-induced conditional deletion of**
369 ***Mmp14* of *Col1a2CreERT2:Mmp14*$^{F/F}$ mice.**
370 **A**, Schematic of *Mmp14* deletion in fibroblasts of *Col1a2CreERT2:Mmp14*$^{F/F}$ (*Mmp14* CKO) mice *in vivo* by
371 tamoxifen-chow feeding at 5 weeks old for 4 weeks. Tissue was collected at T0 (before tamoxifen induction),
372 T1, 2, 3 and 4 (1, 5, 9 and 14 weeks after tamoxifen induction). **B-C**, Photographs showing thickening of skin
373 of *Mmp14* CKO at site-matched locations of the limb. **C**, thickening of tendons in the tail compared to control
374 litter mates at T=4. **D**, Transmission electron microscopy analysis showed *Mmp14* CKO tendons accumulated
375 narrow diameter fibrils both in the matrix and inside cells (black arrows, inset). increase in ~50 nm ⦸ fibrils
376 in *Mmp14* CKO tendons. **E**, Fibril diameter distributions of fibrils measured in control and *Mmp14* CKO
377 tendons at T4 show an increase in narrow-diameter (~50 nm) fibrils in *Mmp14* CKO tendons. **F**, Circularity of
378 collagen fibril cross sections of *Mmp14* CKO tendons showed significant irregularity compared to Ctrl fibrils
379 at all time points after tamoxifen induction, and increasing irregularity over time (270-470 fibrils measured
380 per time point; ***p<0.0001 between Ctrl and CKO, two way ANOVA, Bonferroni post tests; ###p<0.0001
381 comparison within CKO samples, Kruskal-Wallis one way ANOVA and Dunn's Multiple Comparison tests). **G**,
382 Single images selected from step-through Movie 1 and Movie 2 generated from volume-EM analysis of WT
383 and CKO tendons. Scale bar, 1 µm.

384 **Figure 3. Recombinant MT1-MMP cleaves soluble but not fibrillar collagen-I.**
385 **A**, Fibril diameter distribution of collagen fibrils dispersed from mouse Achilles tendons before treatment
386 and 24 h after treatment with and without rhMT1-MMP at 30 °C. *Effective hydrated fibril diameter (>500
387 fibrils measured). **B** Coomassie blue-stained gel showing incubation of monomeric and fibrillar collagen-I
388 with recombinant human MT1-MMP at 30 °C and 37 °C, in the presence or absence of 50 mM EDTA. M,
389 monomeric; F, fibrillar collagen dispersed from Achilles tendon. rhMT1-MMP generated ¾α1(I) and ¾α2(I)
390 fragments from monomeric collagen I (red box) and from fibrillar collagen (white box). Asterisk shows the
391 β-crosslinked chains of collagen-I. A prominent faster migrating β-dimer is seen in the MT1-MMP treated
392 samples which occurs in the presence and absence of 50 mM EDTA. **C**, Mass spectrum of rhMT1-MMP

393 generated fragments from monomeric collagen I shows the mass to charge ratio of individual ions resulting
394 from MS/MS fragmentation pattern between Gly_{775} and Ile_{776}. **D,** Precise fragmentation pattern that
395 contributes to the generation of b and y ions.

396 **Figure 4. Proteomic analysis of tendons from conditionally-deleted *Mmp14* mice.**
397 **A**, Experimental strategy and results summary of proteomics analysis of protein abundance in tendons of
398 *Col1a2CreERT2:Mmp14*$^{F/F}$ (CKO) compared to control littermates at ZT3, when *Mmp14* levels are highest,
399 and at 12 h apart (ZT15) (n=3). 1195 proteins were identified, 212 were identified as significantly time-
400 dependent in control tendons ($p<0.05$), of which 17 remained time-dependent, 19 showed a reversed
401 abundance pattern, and 176 were no longer time-dependent in *Mmp14* CKO tendons. **B**, Heat map
402 representation of proteins that remained time-dependent in *Mmp14* CKO tendons, including proteins with
403 abundance in anti-phase to wild type tendons. **C**, Heat map representation of the abundance of 176 proteins
404 that are time-dependent in control tendons but are no longer time-dependent in *Mmp14* CKO tendons. **D**,
405 Functional analysis of proteins, of which the abundance remains time-dependent in *Mmp14* CKO tendons.
406 The top five significantly ($p<0.05$) enriched gene ontology terms in biological function are shown. Numbers
407 in bars show p values. **E**, Functional analysis of proteins, of which the time-dependent abundance have been
408 deregulated *Mmp14* CKO tendons. The top significantly ($p<0.05$) enriched gene ontology terms in biological
409 function and molecular function are shown. Numbers in bars show p values.

410 **Figure 5. Focal adhesion site formation requires *Mmp14*.**
411 Representative images of control and *Mmp14* KO Per2::Luc iTTFs (**A**) and *Mmp14* KO MC3T3 cells (**B**) stained
412 with phalloidin (magenta) and vinculin (green). Bars represent 10 µm. **C**, percentage of cell spreading on
413 fibronectin after 10 min. Quantification from n=3 independent experiments, a minimum of 2000 cells per
414 replicate were scored. **D**, Numbers of vinculin-positive focal adhesions were counted in control Per2::Luc
415 ITTFs or CRISPR-Cas9 *Mmp14* KO cells, a minimum of 2000 cells were counted per replicate, n=4, the numbers
416 of focal adhesions per cell are reported relative to control iTTFs. **E**) The average focal adhesion size was
417 unaltered in *Mmp14* KO cells although large focal adhesions were less frequently observed. **F**, Confocal
418 microscopy images of control and *Mmp14* KO iTTFs immunolabelled for vinculin and collagen and stained
419 with phalloidin after 72 hrs in culture. Bar, 10 µm. **G,** representative western blot of filamentous actin and
420 soluble globular actin separated through ultra-centrifugation. **H**, Quantification of the F/G actin ratio in
421 *Mmp14* KO cells, n=3. * $p<0.05$, ** $p<0.01$, one-way ANOVA.

422 **Figure 6. Cells with *Mmp14* knockdown have fewer actin filaments and reduced ability to spread.**
423 **A**, Bioluminescence recordings from Per2::Luc iTTFs (black) treated with cytochalasin B for 1 hour prior to
424 dexamethasone synchronisation. **B,** bioluminescence recordings from Per2::Luc iTTFs transduced with
425 control (black) or shRNA targeting vinculin (shVinc, blue) after dexamethasone synchronisation. **C**,
426 Immunofluorescent detection of vinculin and collagen along with actin fibres detected with phalloidin in
427 *Mmp14* knockout cells following addition of 10 µM FAK Inhibitor, PF-573228. **D**, Bioluminescence recordings
428 from Per2::Luc iTTFs without synchronisation (red), after dexamethasone treatment (blue) or after pre-
429 treatment with 10 µM PF-573228 for 5 hours prior to dexamethasone treatment. **E,** FAK inhibition
430 strengthened and prolonged dexamethasone induced circadian rhythms and was also observed in *Mmp14*
431 KO Per2::luc iTTFs

432 **Figure 7. Pitx2 Is elevated in *Mmp14* CKO tendons.**
433 **A,** Real-time PCR detection of Pitx2 mRNA levels in WT and *Mmp14* CKO tail tendons 5 weeks post tamoxifen
434 treatment, at ZT3 (09:00 hr) and ZT15 (21:00 hr). **B,** Real-time PCR of PLOD2 mRNA expression in WT and
435 *Mmp14* CKO tail tendons (n=3 animals per time point) 5 weeks post tamoxifen treatment, at ZT3 (09:00 hr)
436 and ZT15 (21:00 hr). **C,** Per2::Luc iTTFs stably transduced with control or Pitx2-GFP lentivirus, demonstrating
437 enhanced expression of Pitx2 and a concomitant increase in Plod2 mRNA expression **D,** (n=3 and n=5

438 respectively). **E,** Live cell Airyscan imaging of Per2::Luc iTTFs and MMP14 CRISPR-Cas9 KO ITTFs stably
439 transduced with Pitx2-GFP lentivirus. Cells were transiently transduced with mCherry tagged MMP14
440 carrying a silent mutation in the CRISPR-Cas9 PAM site. Pitx2-GFP was readily detected within the nucleus
441 but also with punctate localisation within the cell body in control cell, these correlated with regions also
442 positive for MT1-MMP. Nuclear Pitx2-GFP signals were stronger within *Mmp14* KO cells and also displayed
443 reduced localisation within the cell body. Re-expression of *Mmp14* within knockout cells reduced nuclear
444 Pitx-GFP signals. **F-I,** Real-time PCR demonstrating expression of *Mmp14* in Pitx2-GFP expressing iTTFs, which
445 resulted in reduced Pitx2 and Plod2 mRNA expression, but enhanced Col1a1 mRNA (n=3).

446 **Figure 8. Higher amplitude of circadian clock rhythm in Per2::Luc fibroblasts overexpressing Pitx2.**
447 **A,** Bioluminescence recordings from Per2::Luc iTTFs and the same cells stably overexpressing Pitx2 and Pitx2-
448 GFP after synchronisation with dexamethasone. **B,** bioluminescence recordings from Per2::Luc iTTFs (n=3)
449 and Pitx2 overexpressing fibroblasts that have been transduced with a lentivirus expressing Pitx2.

450 **Extended data figure 1: Depletion or inactivation of *Mmp14* weakens circadian entrainment.**
451 **A**, left, Mmp14 mRNA expression detected by real-time PCR 72 hours after transfection of Per2::Luc iTTFs
452 with scrambled (si-scram) or *Mmp14* targeting siRNA (siMmp14), (n=3 biological replicates), **B,**
453 representative bioluminescence recordings from si-scram and si-MMP14 transfected Per2::Luc fibroblasts,
454 after synchronisation with dexamethasone (n=3 biological replicates). **C,** Dose response curves showing the
455 effects of GM6001 on the viability of Per2::luc iTTFs assessed by Alamar blue. **D,** representative
456 bioluminescence recordings from DMSO or GM6001 treated Per2::Luc fibroblasts, with and without
457 synchronisation with dexamethasone (n=3 biological replicates). **E,** bioluminescence recordings from
458 Per2::Luc iTTFs (black) and CRISPR-Cas9 edited *Mmp14* Per2::Luc fibroblasts (red) after synchronisation with
459 forskolin, **F,** bioluminescence recordings from Per2::Luc iTTFs (black) and CRISPR-Cas9 edited *Mmp14*
460 Per2::Luc fibroblasts (red) after synchronisation with 50% serum shock. **G,** After flow cytometry sorting of
461 Per2::Luc iTTFs transduced with retrovirus expressing scrambled or vinculin targeting shRNA and GFP. GFP
462 positive cells were sorted and mRNA levels of vinculin were assessed by real-time PCR, vinculin mRNA levels
463 relative to control iTTFs are shown (n=3 biological repeats). **H,** Representative images showing the
464 morphology of Per2::Luc iTTFs transduced with scrambled and vinculin targeting shRNA, captured 24 hours
465 after seeding cells onto plastic tissue culture dishes.

466 **Extended data figure 2: *Mmp14*-deficient tendons accumulate D1 collagen fibrils.**
467 Transmission electron microscopy of wildtype (A) and Mmp14 null (B) mouse tail tendons. Scale bar, 0.5 µm.

468 **Extended data figure 3: Depletion or inactivation of *Mmp14* weakens circadian entrainment**
469 **A,** Correlation matrix showing Pearson's R-squared values between datasets resulting from mass
470 spectrometry analysis of tail tendon tissue from *Col1a2CreERT2:Mmp14*$^{F/F}$ (CKO) and control (Ctrl) at ZT3 and
471 ZT15 timepoints within the circadian cycle (n=3 biological repeats; see Figure 4). Greater similarity was
472 observed between samples at different timepoints than between CKO vs. Ctrl. **B,** Plot showing fold-changes
473 in protein abundance, correlating changes observed in *Mmp14* CKO tendon tissues between ZT15 vs. ZT3
474 time points, to changes observed in control tissue between corresponding time points. The data showed
475 significant positive correlation, with a Pearson's R-squared value of 0.2421 ($p < 0.0001$). However, the
476 difference between the ZT15 vs. ZT3 timepoints was compressed in the *Mmp14* cKO tissues, evidenced by
477 linear fit to the data (shown in red, with gradient lower than y=x), and consistent with a dampened circadian
478 response (n=3 biological repeats).

479 **Extended data figure 4: Different protein expression in *Mmp14* CKO.**
480 Plots of proteins that remained time dependent; ECM proteins (COL1A1, COL1A2, COL5A1, FN1),
481 Metalloproteinases (MMP14, TIMP2), Lysyl oxidase (PLOD2, LOXL2), Proteoglycans (DCN, LUM, FMOD, TNC);

482 in tendons of Col1a2CreERT2:Mmp14$^{F/F}$ (CKO) compared to control littermates at ZT3, when *Mmp14* levels
483 are highest, and at 12 hrs apart (ZT15) at T2 (14 weeks old, 5 weeks after tamoxifen chow feeding) (n=3).

484 MATERIALS AND METHODS

485 Mice

486 The care and use of all mice in this study was carried out in accordance with the UK Home Office regulations,
487 UK Animals (Scientific Procedures) Act of 1986 under the Home Office licence (70/8858) and with German
488 legal guidelines. Ethical approval was granted by the University of Manchester and by the
489 Regierungspräsidium Köln, Germany (NRW authorization 50.203.2- K 37a, 20/05 and AZ2010.A342). The
490 permission included the generation of CKO out animals. All mice were housed in 12-h light/12-h dark cycle
491 (LD) and are indicated where zeitgeber time (ZT) is used, with the exception of wild type C57BL/6 mice housed
492 in 12-h dark/12-h dark cycle (DD) that were used for circadian time (CT) time-series microarray and protein
493 extraction as previously described [21]. To generate inducible CKO mice in which *Mmp14* is ablated in
494 fibroblasts upon induction with tamoxifen, we crossed mice expressing CreER recombinase under the control
495 of the *Col1a2* promoter (*Col1a2-CreERT2*; C57BL/6) [59] with C57BL/6 mice carrying the floxed exons (exons 2
496 to 4) of the *Mmp14* gene [60] to produce *Col1a2-CreERT2::Mmp14$^{lox/lox}$* CKO mice. To induce *Mmp14* ablation,
497 mice were fed tamoxifen-formulated chow at 5-weeks old for 4 weeks. To generate mice in which *Bmal1* is
498 ablated in tendon-lineage cells, we crossed mice expressing Cre recombinase under the control of the
499 *Scleraxis* promoter (*Scx-Cre*; C57BL/6) [61] with C57BL/6 mice carrying loxP sites flanking the exon encoding the
500 BMAL1 basic helix-loop-helix domain [62] bred on a background with *PER2::Luciferase* knock-in [18] to produce
501 *Scx-Cre::Bmal1$^{lox/lox}$* KO mice. *Scx-Cre::Bmal1$^{lox/lox}$* KO mice were validated previously [22]. *Col1a1$^{r/r}$* mice were
502 imported from Jackson Laboratory (*B6;129S4-Col1a1$^{tm1Jae/J}$*) [63]. Mice that showed signs of distress or had
503 problems walking were humanely sacrificed using Home Office approved cervical dislocation.

504 RNA isolation and qPCR analysis

505 RNA was isolated from Achilles and tail tendons as described previously [64]. In brief, tissues were washed with
506 ice-cold PBS 3 times and snap frozen in liquid nitrogen with 500 µL TRIzol Reagent (Thermo Fisher Scientific)
507 using a Mikro Dismembrator S (B. Braun Biotech International) at 2000 Hz for 90 seconds two times. After,
508 500 µL TRIzol was added to the homogenized samples and RNA was isolated according to the manufacturer's
509 protocol. DNase treatment of RNA was performed using RQ1 RNase-free DNase (Promega) according to
510 manufacturer's protocol. RNA integrity was assessed by gel electrophoresis and RNA concentration was
511 measured using a NanoDrop 2000 (Thermo Fisher Scientific). TaqMan Reverse Transcription Reagents
512 (Thermo Fisher Scientific) were used for complementary DNA synthesis and SensiFAST SYBR kit reagents
513 (Bioline) were used for qPCR. Primers sequences used were: *Mmp14* AGT GAC AGG CAA GGC TGA TT and
514 GCC CAC CTT AGG GGT GTA AT, and *Gapdh* AAC TTT GGC ATT GTG GAA GG and ACA CAT TGG GGG TAG GAA
515 CA. The $2^{-\Delta\Delta Ct}$ method [65] was used to analyse relative fold changes in gene expression compared to the first
516 time point. Microarray data for *Mmp14* expression during 48 h was collected previously [21] and the data is
517 available on ArrayExpress (accession number E-MTAB-7743).

518 Transmission electron microscopy and morphometric analyses

519 Tendons from mice were prepared for transmission electron microscopy (TEM) as described previously [28].
520 Fibril diameter, perimeter and area were measured using ImageJ software to calculate circularity and fibril
521 volume fraction as described previously [28]. Fibril diameter distributions were plotted and fitted to 3-Gaussian
522 distribution using Sigma Plot 12.0 software (Systat Software) as previously described [28].

523 Western blotting

524 Protein purification and western blot analyses were performed as described previously [22]. Wild type mice
525 were kept in DD for 36 h to allow endogenous circadian rhythm of gene expression. Protein was purified

526 from tail tendons at 4-h intervals. Primary antibodies used were mouse mAb to MT1-MMP (1:500; clone LEM-
527 2/15.8, Millipore) and mAb GAPDH (1:10000; clone Gapdh71.1; Merck).

528 **Sample preparation for proteomic analysis**

529 Tail tendons from wild type and *Mmp14* CKO mice were collected at ZT3 and ZT15. Tissues were homogenized
530 with a bullet blender (with 1.6 mm steel beads; Next Advance) at maximum speed at 4 °C for 5 min in 200 µL
531 of SL-DOC buffer (1.1% sodium laurate, 0.3% sodium deoxycholate, 0.5 mM dithiothreitol (DTT) in 25 mM
532 ammonium bicarbonate), supplemented with protease and phosphatase inhibitor cocktails (Roche). Samples
533 were incubated at 4 °C for 5 min, alkylated with 12 µL of 30 mM of iodoacetamide for 20 min at RT, followed
534 by quenching with 12 µL of 30 mM DTT. Samples were centrifuged at maximum speed for 10 min.
535 Supernatants were transferred into LoBind tubes (Eppendorf) and protein concentrations measured using a
536 Millipore Direct Detect spectrometer. A total of 2 µg protein per sample was digested using trypsin beads in
537 accordance with the manufacturer's protocol (SMART digestion kit, Thermo Scientific). Supernatants were
538 extracted from the beads and 10% formic acid added to adjust to pH 3. Samples were cleaned using an
539 organic phase extraction method: 400 µL ethylacetate (Sigma Aldrich) was added, the resulting solution
540 thoroughly mixed, centrifuged, and the organic phase extracted and discarded; this process was then
541 repeated. Samples were then desalted, in accordance with the manufacturer's protocol, using POROS R3
542 beads (Thermo Fisher) and lyophilized in a speed-vac centrifuge (Heto).

543 **Liquid chromatography-coupled tandem mass spectrometry (LC-MS/MS)**

544 Samples were dissolved in 15 µl of 5% acetonitrile with 0.1% formic acid. Digested samples were analyzed
545 using an UltiMate® 3000 Rapid Separation liquid chromatography system (RSLC, Dionex Corporation) coupled
546 to either Q Exactive HF (Thermo Fisher Scientific) mass spectrometer. Peptides were separated in a gradient
547 of 95% A and 5% B to 7% B at 1 min, 18% B at 58 min, 27% B in 72 min and 60% B at 74 min at 300 nL/min
548 using a 75 mm x 250 µm inner diameter 1.7 µM CSH C18, analytical column (Waters). Peptides were selected
549 for fragmentation automatically by data dependent analysis.

550 **Proteomics data processing**

551 Spectra from multiple samples were aligned using Progenesis QI (Nonlinear Dynamics) Peak-picking
552 sensitivity was set to 4/5 and all other parameters were left as defaults. Only peptides with charge between
553 +1 to +4, with 2 or more isotopes were taken for further analysis. Filtered peptides were identified using
554 Mascot (Matrix Science UK), by searching against the SwissProt and TREMBL mouse databases. The peptide
555 database was modified to search for alkylated cysteine residues (monoisotopic mass change, 57.021 Da),
556 oxidized methionine (15.995 Da), hydroxylation of asparagine, aspartic acid, proline or lysine (15.995 Da) and
557 phosphorylation of serine, tyrosine, threonine, histidine or aspartate (79.966 Da). A maximum of 2 missed
558 cleavages was allowed. Peptide detection intensities were exported from Progenesis QI as Excel (Microsoft)
559 spread sheets for further processing using code written in-house in MATLAB with the bioinformatics toolbox
560 (R2015a, The MathWorks, USA). Raw proteomic data was deposited to the ProteomeXchange Consortium
561 via the PRIDE partner repository with the data set identifier PXD031692. Fold-change differences in the
562 quantity of proteins detected in different samples were calculated by fitting a linear regression model to take
563 into account inter-sample variation [66, 67]. Briefly, peptide intensities were logged and normalised by the
564 median intensity; protein fold-changes were calculated using a mixed-effects linear regression model,
565 considering random (peptides, biological replicates) and fixed (controlled variables) effects. Pathway
566 enrichment analysis was performed using the DAVID bioinformatics resource [31]. Peptide identifications were
567 filtered via Mascot scores so that only those with a Benjamini-Hochberg false discovery rate (FDR) $\geq$ 0.05
568 remained. FDR filtering was performed on combined phospho-enriched and non-enriched datasets as
569 described in [68]. Raw ion intensities from peptides belonging to proteins with fewer than 2 unique peptides
570 (by sequence) per protein in the dataset were excluded from quantification. Remaining intensities were
571 logged and normalized by the median logged peptide intensity. Peptides assigned to different isoforms were

572 grouped into a single "protein group" by gene name. Only peptides observed in at least 2 samples were used
573 in quantification. Missing values were assumed as missing due to low abundance, an assumption others have
574 shown is justified [69]. Imputation was performed at the peptide level following normalization using a method
575 similar to that employed by Perseus [70] whereby missing values were imputed randomly from a normal
576 distribution centered on the apparent limit of detection for this experiment. The limit of detection in this
577 instance was determined by taking the mean of all minimum logged peptide intensities and down-shifting it
578 by 1.6σ, where σ is the standard deviation of minimum logged peptide intensities. The width of this normal
579 distribution was set to 0.3σ as described in [70]. Fold-change differences in the quantity of proteins detected
580 in different time-points were calculated by fitting a mixed-effects linear regression model for each protein
581 with Huber weighting of residuals (doi: 10.1214/aoms/1177703732) as described in [69] using the fitglme
582 Matlab (The MathWorks, USA) function with the formula:

583 $$y_{iptb} = \beta_t + \beta_p + \beta_b$$

584 Where y_{ipt} represents the $\log_2$ (intensity) of peptide p belonging to protein i, at time-point t, in batch b. βs
585 represent effect sizes for the indicated coefficients. Peptide was entered as a random effect whereas time-
586 point was entered as a fixed effect. Standard error estimates were adjusted with Empirical Bayes variance
587 correction according to [71, 72]. Conditions were compared with Student's t-tests with Benjamini-Hochberg
588 correction for false positives (doi:10.1111/j.2517-6161.1995.tb02031.x).

589 **Bioluminescence imaging and recordings**

590 Bioluminescence was recorded as described previously [22]. Briefly, tendon fibroblasts were cultured on 35
591 mm culture dish in recording media containing 0.1 mM luciferin (Merck) in the presence of 100 nM
592 dexamethasone (Merck) and real-time quantitative bioluminescence was recorded using lumiCycle
593 apparatus (Actimetrics). Baseline subtraction was carried out using a 24-hr moving average. Amplitude was
594 calculated as peak-trough difference in bioluminescence of the second peak using base-line subtracted data.

595 **Fusion protein constructs**

596 Lentivirus expression of *Mmp14* was achieved using vectors generated by Vectorbuilder. Murine *Mmp14*
597 coding sequences were expressed under a CMV promoter, with mutation of the *Mmp14* targeting gRNA,
598 AGATCAAGGCCAATGTTCGGAG, PAM site (AGG to AAA). For mCherry tagging the mCherry coding sequence
599 was introduced after amino acid 536 of murine *Mmp14* following the design of Dr. Philippe Chavrier [73], these
600 vectors also carried blasticidin resistance gene. Pitx2GFP expressing cells were cloned into pLenti PGK Neo
601 DEST (Addgene plasmid # 19067 ref[74]), EGFP was cloned at the C terminus of the coding sequence of Pitx2
602 isoform 1 (Origene; MR227617). Lentivirus particles were generated as previously described [75]. Stable cells
603 were created by neomycin selection (250 µg/mL) or 5 µg/mL blasticidin.

604 **Light microscopy**

605 Live cell super resolution microscopy for **Figure 7** was performed using a Zeiss LSM 880 Axio Observer
606 microscope with Airyscan detection system in SR mode using a Plan-Apochromat 63×/1.4 Oil DIC M27
607 objective (Carl Zeiss, Jena, Germany). Excitation was achieved using the 488 nm line from an argon laser and
608 594 nm HeNe laser and emitted light was collected through appropriate filters to eliminate any spill-over.
609 Raw images were Airyscan processed using the default settings and analyzed using ZEN 2.1 software and the
610 image brightness and contrast adjusted using BestFit.

611 **CRISPR/Cas9**

612 To generate *Mmp14* knockout fibroblasts, immortalized tail tendon fibroblasts from the Per2::Luc mouse,
613 generated at previously described [76], were transduced with lentivirus particles created from vectors co-
614 expressing Cas9 and gRNA (ABMgood 302361140595). *Mmp14* knockout were achieved using vectors
615 encoding the gRNA AGATCAAGGCCAATGTTCGGAG. After puromycin selection (2.5 µg/mL) we isolated single
616 cell clones by FACS and confirmed knockout of *Mmp14* by real-time PCR and western blotting.

617 **Collagen content and crosslink analyses**

618 The hydroxylysine aldehyde (pyridinoline) cross-link content of tendon samples was determined by HPLC
619 after acid hydrolysis in 6 N HCl for 24 hrs at 108 °C as previously described [34]. Results were expressed in
620 residues per mole of collagen based on the hydroxyproline content assayed on the same hydrolysate as a
621 measure of tissue collagen content.

622 **Statistical analysis**

623 Data were evaluated using Two-tailed Student's t-test, two-way ANOVA or non-parametric, two-tailed Mann-
624 Whitney test. Results were presented as mean ± SEM from at least three independent experiments.
625 Differences were considered significant at the values of *P < 0.05, **P < 0.01 and ***P < 0.001.

626 **REFERENCES**

627

628 1. Sato, H. *et al.* A matrix metalloproteinase expressed on the surface of invasive tumour cells. *Nature*
629 **370**, 61-65 (1994).
630 2. Tam, E.M., Morrison, C.J., Wu, Y.I., Stack, M.S. & Overall, C.M. Membrane protease proteomics:
631 Isotope-coded affinity tag MS identification of undescribed MT1-matrix metalloproteinase
632 substrates. *Proc Natl Acad Sci U S A* **101**, 6917-6922 (2004).
633 3. Hotary, K.B. *et al.* Membrane type I matrix metalloproteinase usurps tumor growth control imposed
634 by the three-dimensional extracellular matrix. *Cell* **114**, 33-45 (2003).
635 4. Sodek, K.L., Ringuette, M.J. & Brown, T.J. MT1-MMP is the critical determinant of matrix degradation
636 and invasion by ovarian cancer cells. *Br J Cancer* **97**, 358-367 (2007).
637 5. Ellerbroek, S.M., Wu, Y.I., Overall, C.M. & Stack, M.S. Functional interplay between type I collagen
638 and cell surface matrix metalloproteinase activity. *J Biol Chem* **276**, 24833-24842 (2001).
639 6. Holmbeck, K., Bianco, P., Yamada, S. & Birkedal-Hansen, H. MT1-MMP: a tethered collagenase. *J Cell*
640 *Physiol* **200**, 11-19 (2004).
641 7. Itoh, Y. Membrane-type matrix metalloproteinases: Their functions and regulations. *Matrix Biol* **44-**
642 **46**, 207-223 (2015).
643 8. Tam, E.M., Wu, Y.I., Butler, G.S., Stack, M.S. & Overall, C.M. Collagen binding properties of the
644 membrane type-1 matrix metalloproteinase (MT1-MMP) hemopexin C domain. The ectodomain of
645 the 44-kDa autocatalytic product of MT1-MMP inhibits cell invasion by disrupting native type I
646 collagen cleavage. *J Biol Chem* **277**, 39005-39014 (2002).
647 9. Holmbeck, K. *et al.* MT1-MMP-deficient mice develop dwarfism, osteopenia, arthritis, and
648 connective tissue disease due to inadequate collagen turnover. *Cell* **99**, 81-92 (1999).
649 10. Zhou, Z. *et al.* Impaired endochondral ossification and angiogenesis in mice deficient in membrane-
650 type matrix metalloproteinase I. *Proc Natl Acad Sci U S A* **97**, 4052-4057 (2000).
651 11. Hiraoka, N., Allen, E., Apel, I.J., Gyetko, M.R. & Weiss, S.J. Matrix metalloproteinases regulate
652 neovascularization by acting as pericellular fibrinolysins. *Cell* **95**, 365-377 (1998).
653 12. Chun, T.H. *et al.* A pericellular collagenase directs the 3-dimensional development of white adipose
654 tissue. *Cell* **125**, 577-591 (2006).
655 13. Taylor, S.H. *et al.* Matrix metalloproteinase 14 is required for fibrous tissue expansion. *Elife* **4**,
656 e09345 (2015).
657 14. Shimizu-Hirota, R. *et al.* MT1-MMP regulates the PI3Kdelta.Mi-2/NuRD-dependent control of
658 macrophage immune function. *Genes Dev* **26**, 395-413 (2012).
659 15. Mu, D. *et al.* The integrin alpha(v)beta8 mediates epithelial homeostasis through MT1-MMP-
660 dependent activation of TGF-beta1. *J Cell Biol* **157**, 493-507 (2002).
661 16. Shi, F. & Sottile, J. MT1-MMP regulates the turnover and endocytosis of extracellular matrix
662 fibronectin. *J Cell Sci* **124**, 4039-4050 (2011).
663 17. Yagita, K., Tamanini, F., van Der Horst, G.T. & Okamura, H. Molecular mechanisms of the biological
664 clock in cultured fibroblasts. *Science* **292**, 278-281 (2001).
665 18. Yoo, S.H. *et al.* PERIOD2::LUCIFERASE real-time reporting of circadian dynamics reveals persistent
666 circadian oscillations in mouse peripheral tissues. *Proc Natl Acad Sci U S A* **101**, 5339-5346 (2004).

667 19. Roenneberg, T. & Merrow, M. Circadian clocks - the fall and rise of physiology. *Nat Rev Mol Cell Biol*
668 **6**, 965-971 (2005).
669 20. Cermakian, N. & Sassone-Corsi, P. Multilevel regulation of the circadian clock. *Nat Rev Mol Cell Biol*
670 **1**, 59-67 (2000).
671 21. Yeung, C.Y. *et al.* Gremlin-2 is a BMP antagonist that is regulated by the circadian clock. *Sci Rep* **4**,
672 5183 (2014).
673 22. Chang, J. *et al.* Circadian control of the secretory pathway maintains collagen homeostasis. *Nat Cell*
674 *Biol* **22**, 74-86 (2020).
675 23. Aggarwal, A. *et al.* The Circadian Clock Regulates Adipogenesis by a Per3 Crosstalk Pathway to Klf15.
676 *Cell Rep* **21**, 2367-2375 (2017).
677 24. Keller, M. *et al.* A circadian clock in macrophages controls inflammatory immune responses. *Proc*
678 *Natl Acad Sci U S A* **106**, 21407-21412 (2009).
679 25. Jensen, L.D. *et al.* Opposing effects of circadian clock genes bmal1 and period2 in regulation of VEGF-
680 dependent angiogenesis in developing zebrafish. *Cell Rep* **2**, 231-241 (2012).
681 26. Pizarro, A., Hayer, K., Lahens, N.F. & Hogenesch, J.B. CircaDB: a database of mammalian circadian
682 gene expression profiles. *Nucleic Acids Res* **41**, D1009-1013 (2013).
683 27. Zigrino, P. *et al.* Fibroblast-Derived MMP-14 Regulates Collagen Homeostasis in Adult Skin. *J Invest*
684 *Dermatol* **136**, 1575-1583 (2016).
685 28. Starborg, T. *et al.* Using transmission electron microscopy and 3View to determine collagen fibril size
686 and three-dimensional organization. *Nat Protoc* **8**, 1433-1448 (2013).
687 29. Itoh, Y. *et al.* A common SNP risk variant MT1-MMP causative for Dupuytren's disease has a specific
688 defect in collagenolytic activity. *Matrix Biol* **97**, 20-39 (2021).
689 30. Sherratt, M.J., Graham, H.K., Kielty, C.M. & Holmes, D.F. Mass-mapping of ECM macromolecules by
690 scanning transmission electron microscopy. *Methods Mol Biol* **522**, 151-161 (2009).
691 31. Huang da, W., Sherman, B.T. & Lempicki, R.A. Systematic and integrative analysis of large gene lists
692 using DAVID bioinformatics resources. *Nat Protoc* **4**, 44-57 (2009).
693 32. Hoyle, N.P. *et al.* Circadian actin dynamics drive rhythmic fibroblast mobilization during wound
694 healing. *Sci Transl Med* **9** (2017).
695 33. Fife, C.M., McCarroll, J.A. & Kavallaris, M. Movers and shakers: cell cytoskeleton in cancer
696 metastasis. *Br J Pharmacol* **171**, 5507-5523 (2014).
697 34. Hudson, D.M. *et al.* Age-related type I collagen modifications reveal tissue-defining differences
698 between ligament and tendon. *Matrix Biol Plus* **12**, 100070 (2021).
699 35. Chakravarti, S. *et al.* Lumican regulates collagen fibril assembly: skin fragility and corneal opacity in
700 the absence of lumican. *J Cell Biol* **141**, 1277-1286 (1998).
701 36. Kalamajski, S. *et al.* Increased C-telopeptide cross-linking of tendon type I collagen in fibromodulin-
702 deficient mice. *J Biol Chem* **289**, 18873-18879 (2014).
703 37. Ghosh, P., Saha, S.K., Nandi, S.S., Bhattacharya, S. & Roy, S.S. Involvement of Pitx2, a homeodomain
704 transcription factor, in hypothyroidism associated reproductive disorders. *Cell Physiol Biochem* **20**,
705 887-898 (2007).
706 38. Hjalt, T.A., Amendt, B.A. & Murray, J.C. PITX2 regulates procollagen lysyl hydroxylase (PLOD) gene
707 expression: implications for the pathology of Rieger syndrome. *J Cell Biol* **152**, 545-552 (2001).
708 39. Hendee, K.E. *et al.* PITX2 deficiency and associated human disease: insights from the zebrafish
709 model. *Hum Mol Genet* **27**, 1675-1695 (2018).
710 40. Tao, G. *et al.* Pitx2 promotes heart repair by activating the antioxidant response after cardiac injury.
711 *Nature* **534**, 119-123 (2016).
712 41. Takahashi, J.S. Transcriptional architecture of the mammalian circadian clock. *Nat Rev Genet* **18**,
713 164-179 (2017).
714 42. Yamamoto, T. *et al.* Transcriptional oscillation of canonical clock genes in mouse peripheral tissues.
715 *BMC Mol Biol* **5**, 18 (2004).
716 43. Li, X. *et al.* CirGRDB: a database for the genome-wide deciphering circadian genes and regulators.
717 *Nucleic Acids Res* **46**, D64-D70 (2018).
718 44. Schwanhausser, B. *et al.* Corrigendum: Global quantification of mammalian gene expression control.
719 *Nature* **495**, 126-127 (2013).

720 45. Schwanhausser, B. *et al.* Global quantification of mammalian gene expression control. *Nature* **473**,
721 337-342 (2011).
722 46. Shoji, K., Ohashi, K., Sampei, K., Oikawa, M. & Mizuno, K. Cytochalasin D acts as an inhibitor of the
723 actin-cofilin interaction. *Biochem Biophys Res Commun* **424**, 52-57 (2012).
724 47. Orgel, J.P. *et al.* Collagen fibril surface displays a constellation of sites capable of promoting fibril
725 assembly, stability, and hemostasis. *Connect Tissue Res* **52**, 18-24 (2011).
726 48. Motrescu, E.R. *et al.* Matrix metalloproteinase-11/stromelysin-3 exhibits collagenolytic function
727 against collagen VI under normal and malignant conditions. *Oncogene* **27**, 6347-6355 (2008).
728 49. Pei, D. & Weiss, S.J. Furin-dependent intracellular activation of the human stromelysin-3 zymogen.
729 *Nature* **375**, 244-247 (1995).
730 50. Nagase, H., Enghild, J.J., Suzuki, K. & Salvesen, G. Stepwise activation mechanisms of the precursor of
731 matrix metalloproteinase 3 (stromelysin) by proteinases and (4-aminophenyl)mercuric acetate.
732 *Biochemistry* **29**, 5783-5789 (1990).
733 51. Okamoto, T. *et al.* Activation of matrix metalloproteinases by peroxynitrite-induced protein S-
734 glutathiolation via disulfide S-oxide formation. *J Biol Chem* **276**, 29596-29602 (2001).
735 52. Galvez, B.G. *et al.* Caveolae are a novel pathway for membrane-type 1 matrix metalloproteinase
736 traffic in human endothelial cells. *Mol Biol Cell* **15**, 678-687 (2004).
737 53. Bassiouni, W., Ali, M.A.M. & Schulz, R. Multifunctional intracellular matrix metalloproteinases:
738 implications in disease. *FEBS J* (2021).
739 54. Kalamajski, S. & Oldberg, A. Homologous sequence in lumican and fibromodulin leucine-rich repeat
740 5-7 competes for collagen binding. *J Biol Chem* **284**, 534-539 (2009).
741 55. Kalamajski, S. & Oldberg, A. The role of small leucine-rich proteoglycans in collagen fibrillogenesis.
742 *Matrix Biol* **29**, 248-253 (2010).
743 56. Engebretsen, K.V. *et al.* Lumican is increased in experimental and clinical heart failure, and its
744 production by cardiac fibroblasts is induced by mechanical and proinflammatory stimuli. *FEBS J* **280**,
745 2382-2398 (2013).
746 57. Mohammadzadeh, N. *et al.* The extracellular matrix proteoglycan lumican improves survival and
747 counteracts cardiac dilatation and failure in mice subjected to pressure overload. *Sci Rep* **9**, 9206
748 (2019).
749 58. Wynn, T.A. Common and unique mechanisms regulate fibrosis in various fibroproliferative diseases. *J*
750 *Clin Invest* **117**, 524-529 (2007).
751 59. Zheng, B., Zhang, Z., Black, C.M., de Crombrugghe, B. & Denton, C.P. Ligand-dependent genetic
752 recombination in fibroblasts : a potentially powerful technique for investigating gene function in
753 fibrosis. *Am J Pathol* **160**, 1609-1617 (2002).
754 60. Zigrino, P. *et al.* Loss of epidermal MMP-14 expression interferes with angiogenesis but not with re-
755 epithelialization. *Eur J Cell Biol* **91**, 748-756 (2012).
756 61. Blitz, E., Sharir, A., Akiyama, H. & Zelzer, E. Tendon-bone attachment unit is formed modularly by a
757 distinct pool of Scx- and Sox9-positive progenitors. *Development* **140**, 2680-2690 (2013).
758 62. Storch, K.F. *et al.* Intrinsic circadian clock of the mammalian retina: importance for retinal processing
759 of visual information. *Cell* **130**, 730-741 (2007).
760 63. Liu, X. *et al.* A targeted mutation at the known collagenase cleavage site in mouse type I collagen
761 impairs tissue remodeling. *J Cell Biol* **130**, 227-237 (1995).
762 64. Yeung, C.Y. *et al.* Chick tendon fibroblast transcriptome and shape depend on whether the cell has
763 made its own collagen matrix. *Sci Rep* **5**, 13555 (2015).
764 65. Livak, K.J. & Schmittgen, T.D. Analysis of relative gene expression data using real-time quantitative
765 PCR and the 2(-Delta Delta C(T)) Method. *Methods* **25**, 402-408 (2001).
766 66. Mallikarjun, V., Richardson, S.M. & Swift, J. BayesENproteomics: Bayesian Elastic Nets for
767 Quantification of Peptidoforms in Complex Samples. *J Proteome Res* **19**, 2167-2184 (2020).
768 67. Gilbert, H.T.J. *et al.* Nuclear decoupling is part of a rapid protein-level cellular response to high-
769 intensity mechanical loading. *Nat Commun* **10**, 4149 (2019).
770 68. Bekker-Jensen, D.B. *et al.* An Optimized Shotgun Strategy for the Rapid Generation of
771 Comprehensive Human Proteomes. *Cell Syst* **4**, 587-599 e584 (2017).

69. Goeminne, L.J., Gevaert, K. & Clement, L. Peptide-level Robust Ridge Regression Improves Estimation, Sensitivity, and Specificity in Data-dependent Quantitative Label-free Shotgun Proteomics. *Mol Cell Proteomics* **15**, 657-668 (2016).
70. Tyanova, S., Temu, T. & Cox, J. The MaxQuant computational platform for mass spectrometry-based shotgun proteomics. *Nat Protoc* **11**, 2301-2319 (2016).
71. Smyth, G.K. Linear models and empirical bayes methods for assessing differential expression in microarray experiments. *Stat Appl Genet Mol Biol* **3**, Article3 (2004).
72. Kammers, K., Cole, R.N., Tiengwe, C. & Ruczinski, I. Detecting Significant Changes in Protein Abundance. *EuPA Open Proteom* **7**, 11-19 (2015).
73. Rosse, C. *et al.* Control of MT1-MMP transport by atypical PKC during breast-cancer progression. *Proc Natl Acad Sci U S A* **111**, E1872-1879 (2014).
74. Campeau, E. *et al.* A versatile viral system for expression and depletion of proteins in mammalian cells. *PLoS One* **4**, e6529 (2009).
75. Calverley, B.C., Kadler, K.E. & Pickard, A. Dynamic High-Sensitivity Quantitation of Procollagen-I by Endogenous CRISPR-Cas9 NanoLuciferase Tagging. *Cells* **9** (2020).
76. Pickard, A. *et al.* Preservation of circadian rhythms by the protein folding chaperone, BiP. *FASEB J* **33**, 7479-7489 (2019).

Figure 1

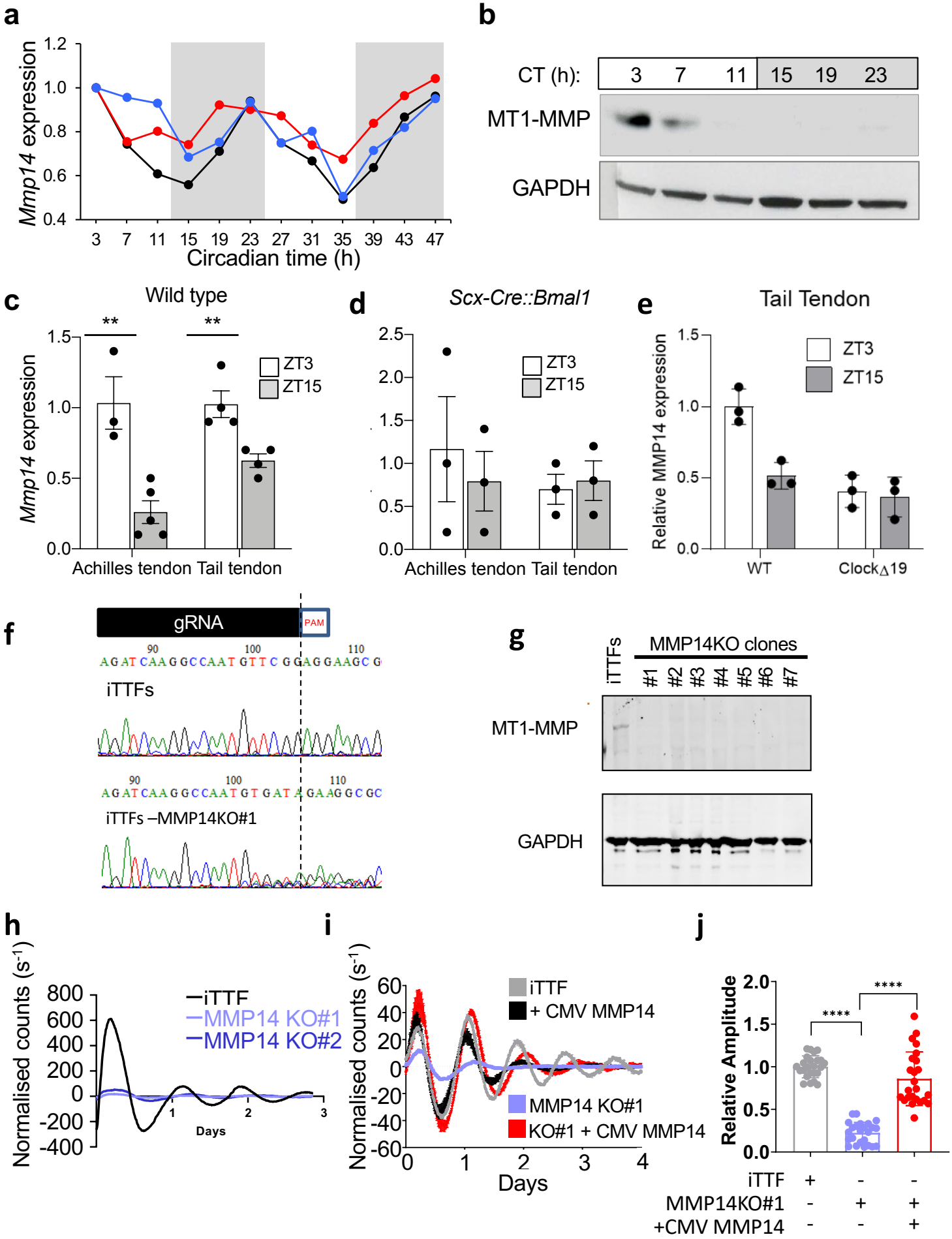
a
Mmp14 expression
1.2
1.0
0.8
0.6
0.4
3 7 11 15 19 23 27 31 35 39 43 47
Circadian time (h)
b
CT (h):
3 7 11 15 19 23
MT1-MMP
GAPDH
c
Wild type
Mmp14 expression
**
**
ZT3
ZT15
Achilles tendon Tail tendon
d
Scx-Cre::Bmal1
ZT3
ZT15
Achilles tendon Tail tendon
e
Tail Tendon
Relative MMP14 expression
ZT3
ZT15
WT
Clock Δ19
f
gRNA
PAM
90 100 110
AGATCAAGGCCAATGTTCGGAGGAAGCG
iTTFs
90 100 110
AGATCAAGGCCAATGTGATAGAAGGCGC
iTTFs –MMP14KO#1
g
iTTFs
MMP14KO clones
#1 #2 #3 #4 #5 #6 #7
MT1-MMP
GAPDH
h
Normalised counts (s-1)
iTTF
MMP14 KO#1
MMP14 KO#2
Days
i
Normalised counts (s-1)
iTTF
+ CMV MMP14
MMP14 KO#1
KO#1 + CMV MMP14
Days
j
Relative Amplitude
****
****
iTTF + - -
MMP14KO#1 - + +
+CMV MMP14 - - +

Figure 2

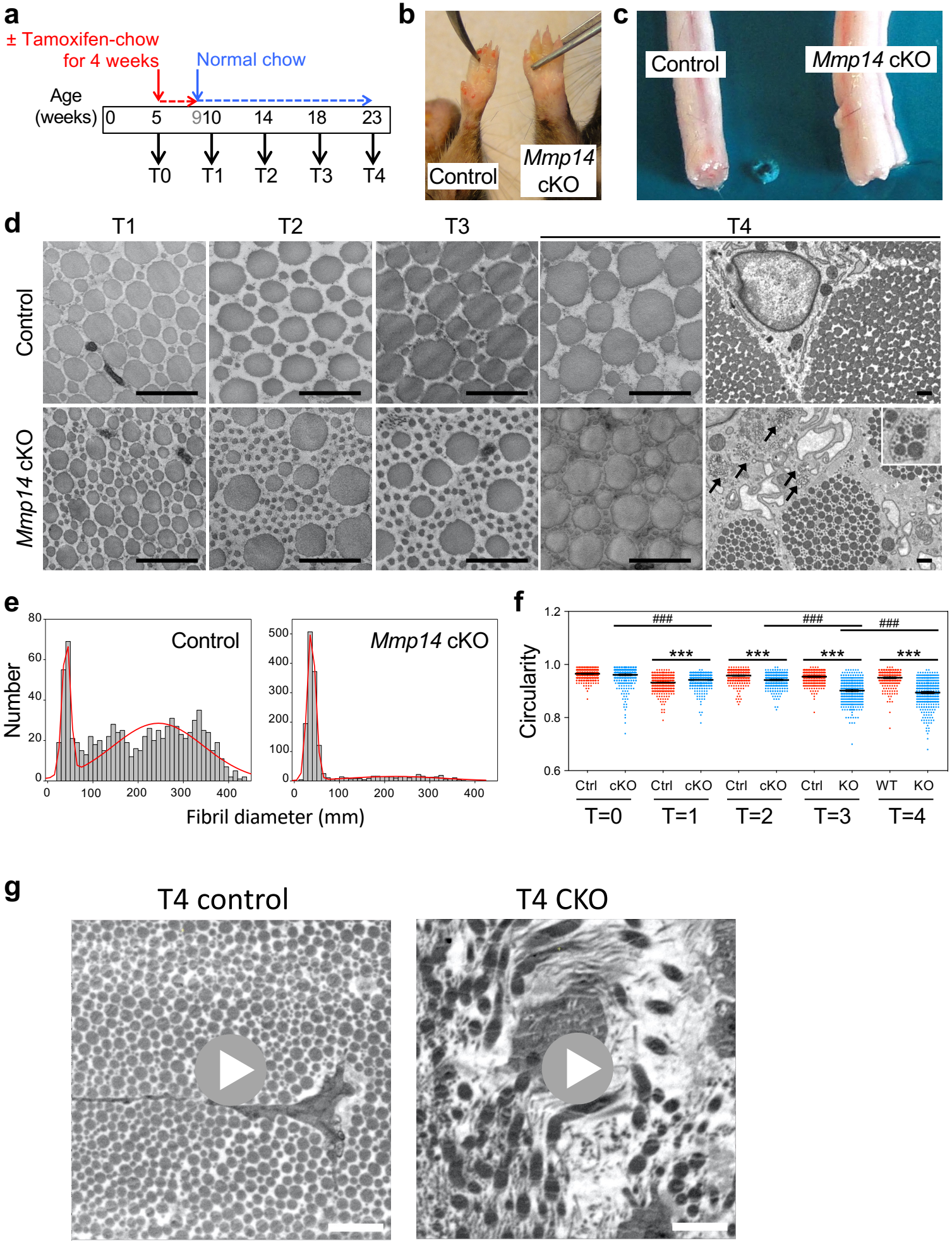
a
± Tamoxifen-chow
for 4 weeks
Normal chow
Age
(weeks)
0
5
910
14
18
23
T0
T1
T2
T3
T4
b
Control
Mmp14
cKO
c
Control
Mmp14 cKO
d
T1
T2
T3
T4
Control
Mmp14 cKO
e
Control
Mmp14 cKO
Number
Fibril diameter (mm)
f
Circularity
###
***
Ctrl
cKO
Ctrl
cKO
Ctrl
cKO
Ctrl
KO
WT
KO
T=0
T=1
T=2
T=3
T=4
g
T4 control
T4 CKO

Figure 3

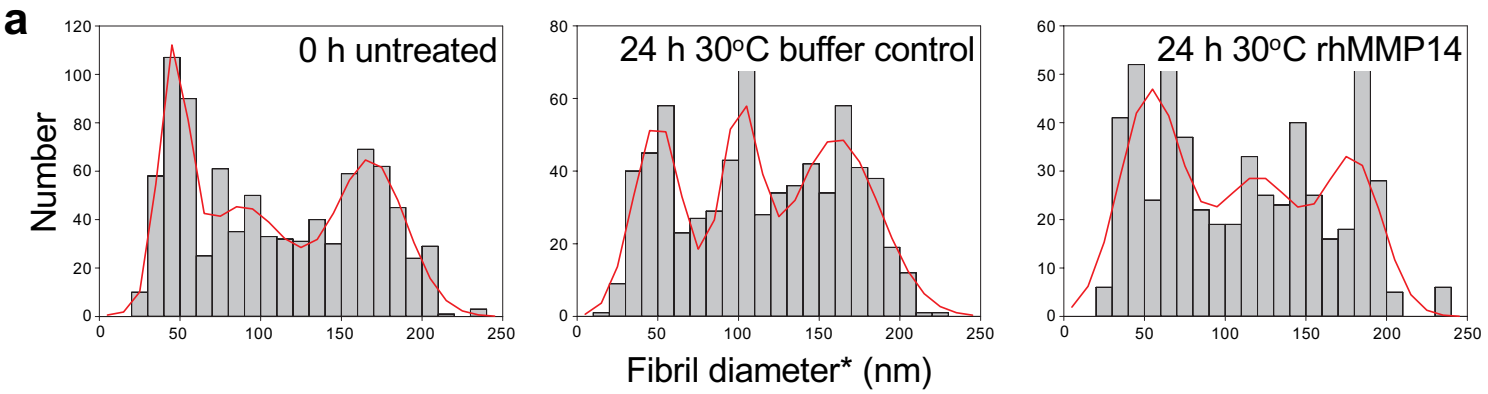
a
0 h untreated
24 h 30°C buffer control
24 h 30°C rhMMP14
Number
Fibril diameter* (nm)

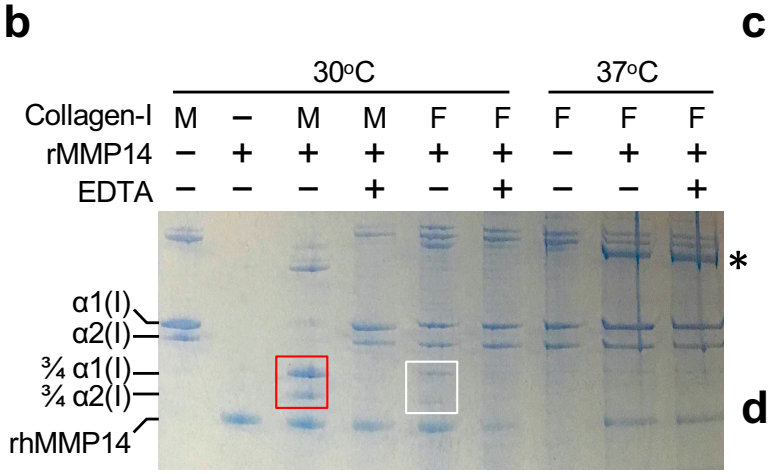
b
30°C
37°C
Collagen-I M – M M F F F F F
rMMP14 – + + + + + – + +
EDTA – – – + – + – – +
α1(I)
α2(I)
¾ α1(I)
¾ α2(I)
rhMMP14
*

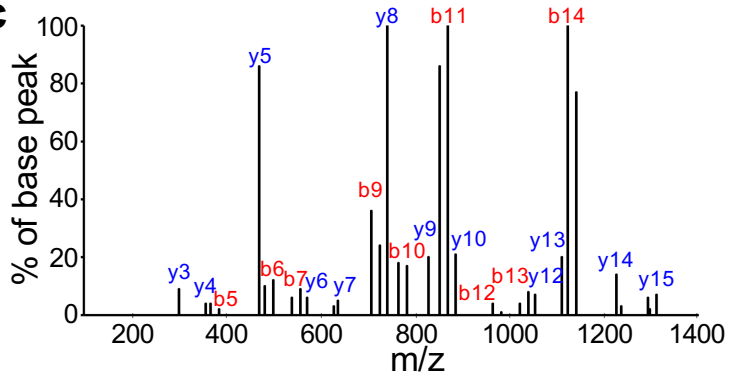
c
% of base peak
m/z
y5
y8
b11
b14
b9
y9
y10
b10
y13
y14
y15
y3
y4
b5
b6
b7
y6
y7
b12
b13
y12

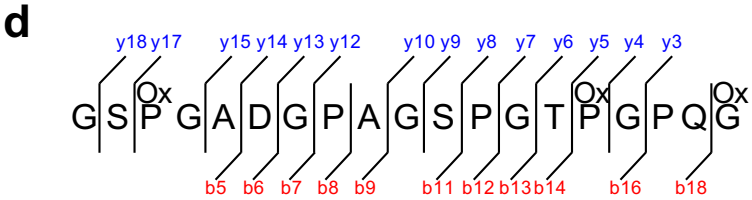
d
y18 y17 y15 y14 y13 y12 y10 y9 y8 y7 y6 y5 y4 y3
G S P Ox G A D G P A G S P G T P Ox G P Q G Ox
b5 b6 b7 b8 b9 b11 b12 b13 b14 b16 b18

Figure 4

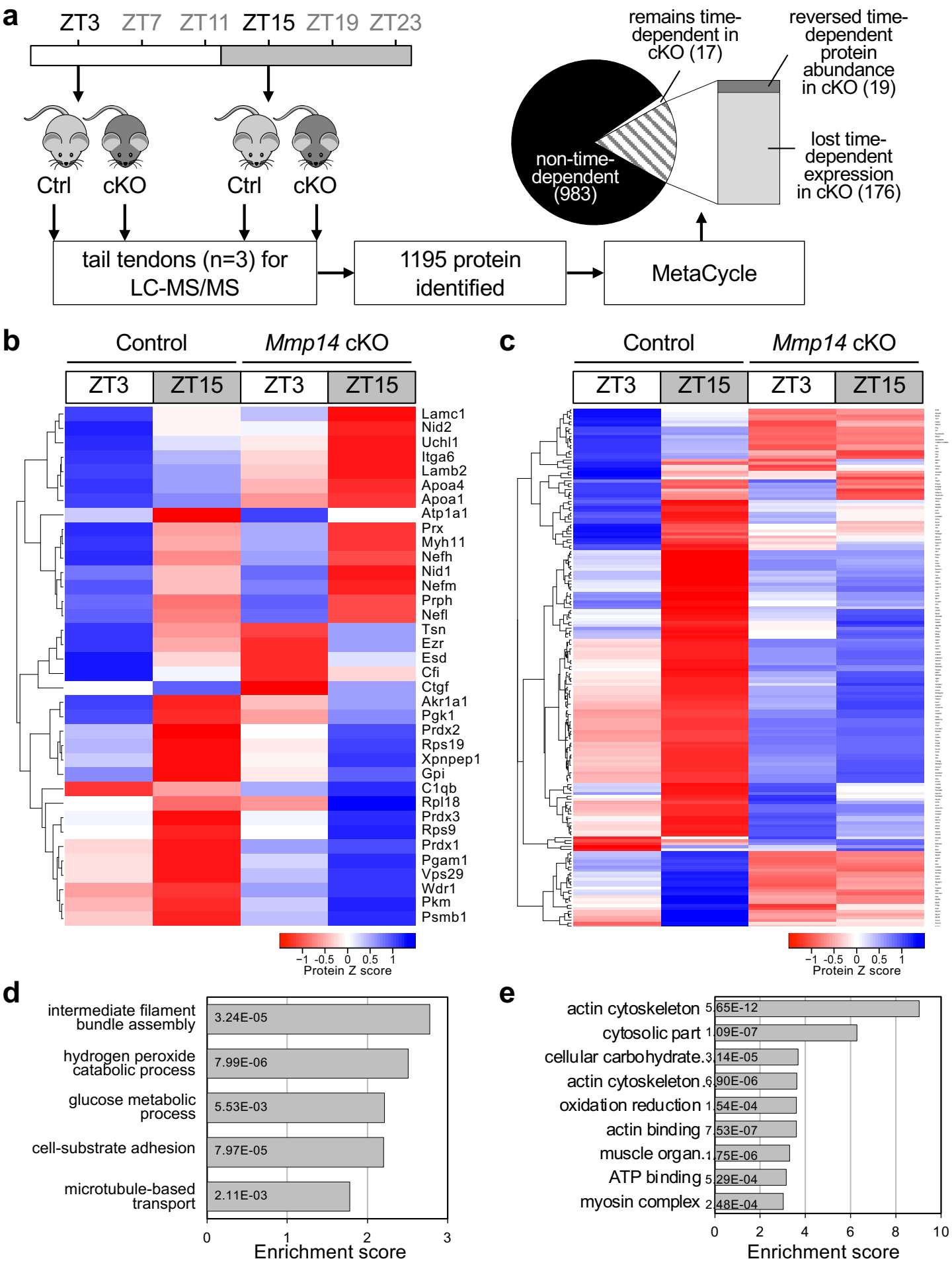
a
ZT3 ZT7 ZT11 ZT15 ZT19 ZT23
Ctrl cKO Ctrl cKO
tail tendons (n=3) for LC-MS/MS
1195 protein identified
MetaCycle
remains time-dependent in cKO (17)
reversed time-dependent protein abundance in cKO (19)
lost time-dependent expression in cKO (176)
non-time-dependent (983)
b
Control
Mmp14 cKO
ZT3 ZT15 ZT3 ZT15
Lamc1
Nid2
Uchl1
Itga6
Lamb2
Apoa4
Apoa1
Atp1a1
Prx
Myh11
Nefh
Nid1
Nefm
Prph
Nefl
Tsn
Ezr
Esd
Cfi
Ctgf
Akr1a1
Pgk1
Prdx2
Rps19
Xpnpep1
Gpi
C1qb
Rpl18
Prdx3
Rps9
Prdx1
Pgam1
Vps29
Wdr1
Pkm
Psmb1
−1 -0.5 0 0.5 1
Protein Z score
c
Control
Mmp14 cKO
ZT3 ZT15 ZT3 ZT15
−1 -0.5 0 0.5 1
Protein Z score
d
intermediate filament bundle assembly
3.24E-05
hydrogen peroxide catabolic process
7.99E-06
glucose metabolic process
5.53E-03
cell-substrate adhesion
7.97E-05
microtubule-based transport
2.11E-03
0 1 2 3
Enrichment score
e
actin cytoskeleton 5.65E-12
cytosolic part 1.09E-07
cellular carbohydrate.3.14E-05
actin cytoskeleton.6.90E-06
oxidation reduction 1.54E-04
actin binding 7.53E-07
muscle organ.1.75E-06
ATP binding 5.29E-04
myosin complex 2.48E-04
0 2 4 6 8 10
Enrichment score

Figure 5

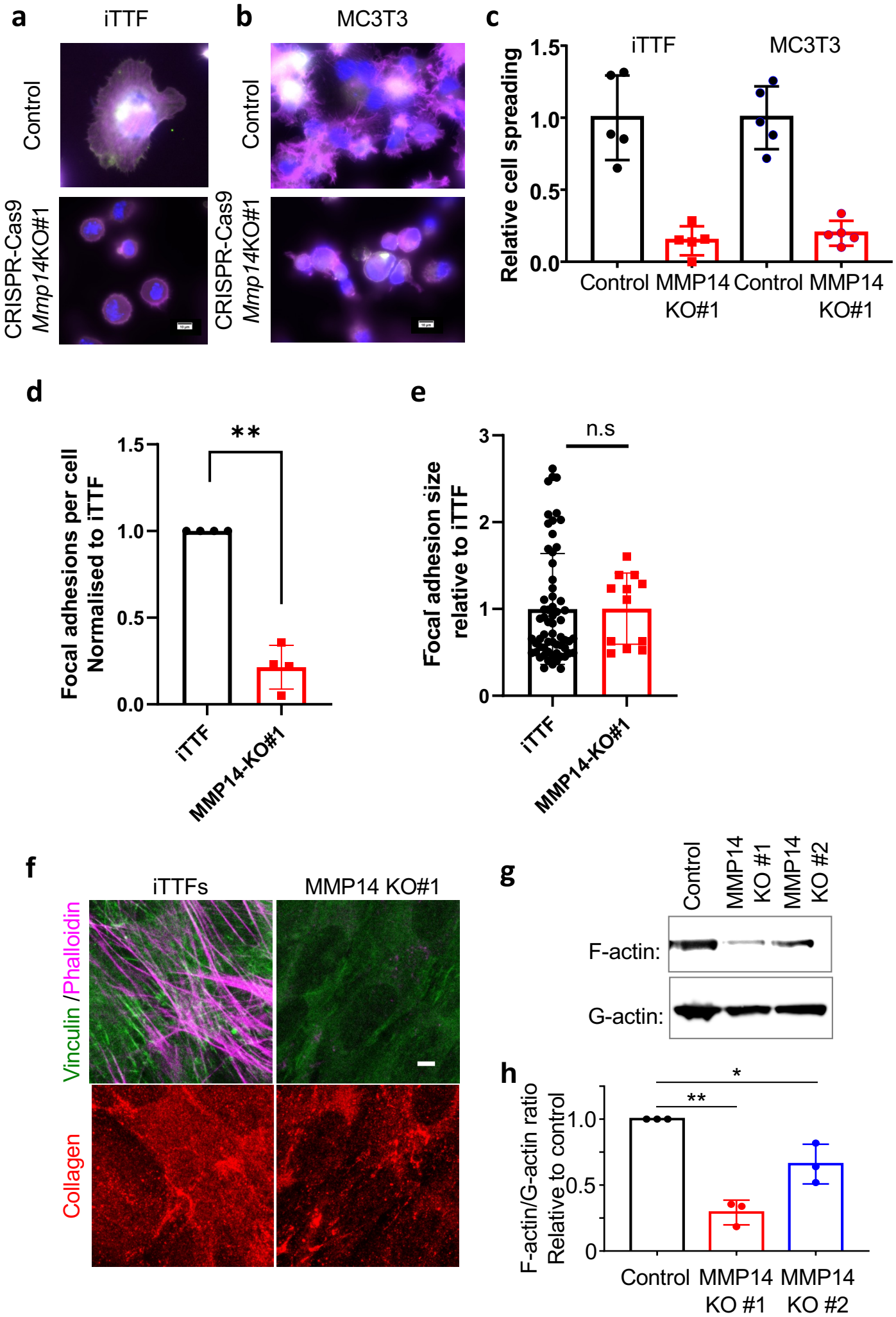
a
iTTF
Control
CRISPR-Cas9 Mmp14KO#1
b
MC3T3
Control
CRISPR-Cas9 Mmp14KO#1
c
iTTF
MC3T3
Relative cell spreading
1.5
1.0
0.5
0.0
Control
MMP14 KO#1
Control
MMP14 KO#1
d
Focal adhesions per cell Normalised to iTTF
**
1.5
1.0
0.5
0.0
iTTF
MMP14-KO#1
e
Focal adhesion size relative to iTTF
n.s
3
2
1
0
iTTF
MMP14-KO#1
f
iTTFs
MMP14 KO#1
Vinculin /Phalloidin
Collagen
g
Control
MMP14 KO #1
MMP14 KO #2
F-actin:
G-actin:
h
F-actin/G-actin ratio Relative to control
*
**
1.0
0.5
0
Control
MMP14 KO #1
MMP14 KO #2

Figure 6

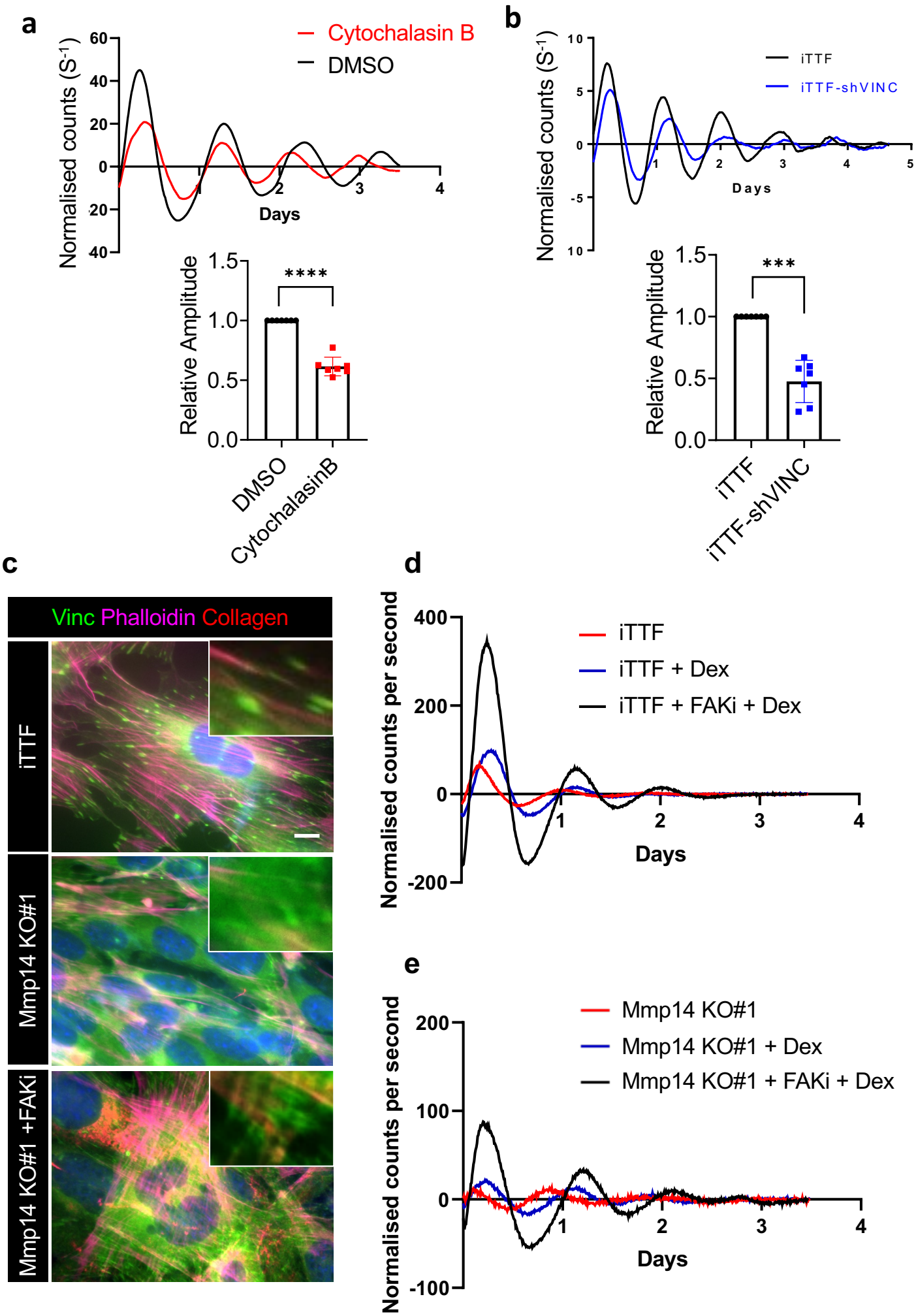
a
Cytochalasin B
DMSO
Normalised counts (S-1)
Days
Relative Amplitude
****
DMSO
CytochalasinB
b
iTTF
iTTF-shVINC
Normalised counts (S-1)
Days
Relative Amplitude
***
iTTF
iTTF-shVINC
c
Vinc Phalloidin Collagen
iTTF
Mmp14 KO#1
Mmp14 KO#1 +FAKi
d
iTTF
iTTF + Dex
iTTF + FAKi + Dex
Normalised counts per second
Days
e
Mmp14 KO#1
Mmp14 KO#1 + Dex
Mmp14 KO#1 + FAKi + Dex
Normalised counts per second
Days

Figure 7

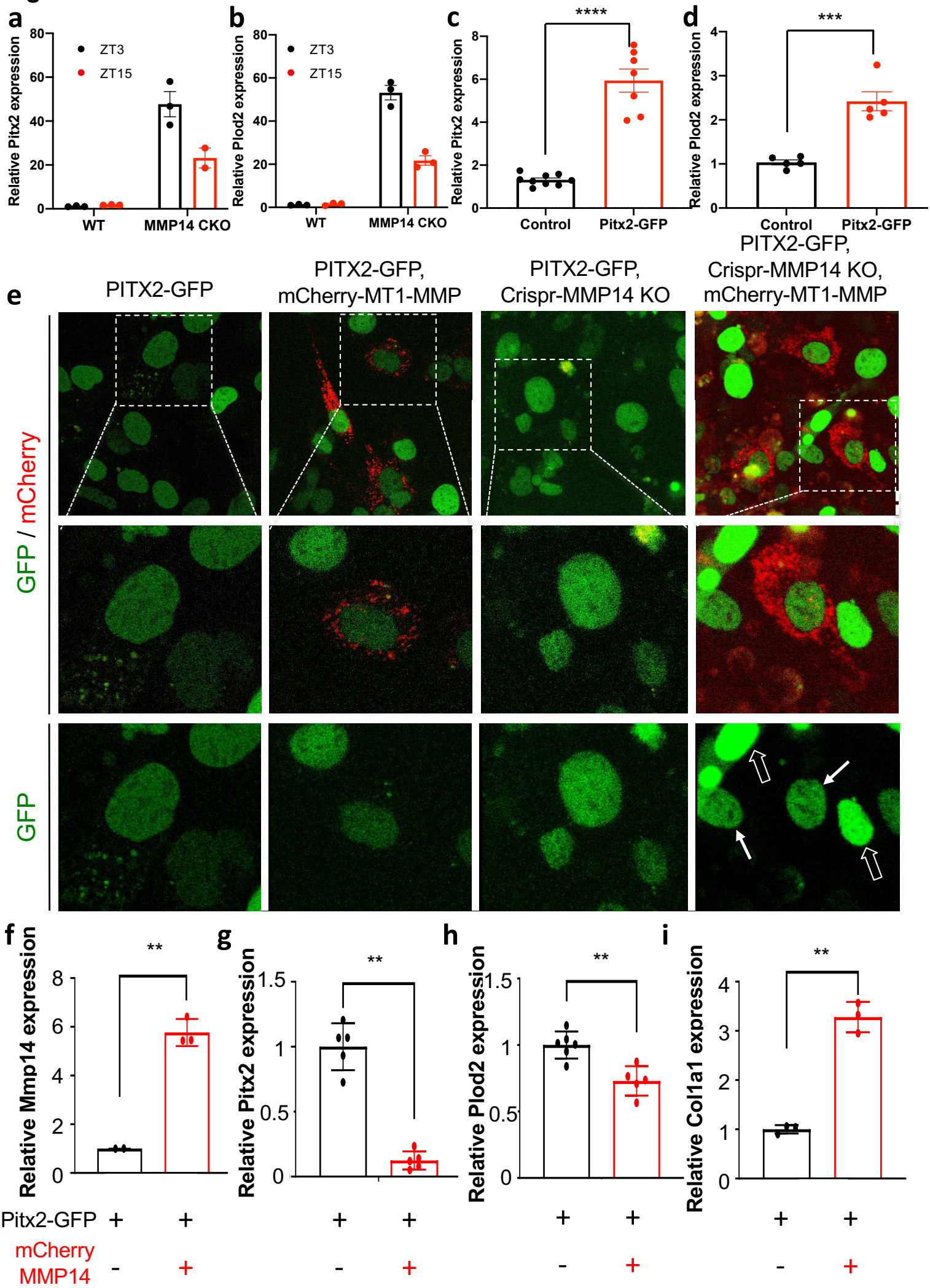
a
Relative Pitx2 expression
ZT3
ZT15
WT
MMP14 CKO
b
Relative Plod2 expression
ZT3
ZT15
WT
MMP14 CKO
c
****
Relative Pitx2 expression
Control
Pitx2-GFP
d
***
Relative Plod2 expression
Control
Pitx2-GFP
e
PITX2-GFP
PITX2-GFP, mCherry-MT1-MMP
PITX2-GFP, Crispr-MMP14 KO
PITX2-GFP, Crispr-MMP14 KO, mCherry-MT1-MMP
GFP / mCherry
GFP
f
**
Relative Mmp14 expression
g
**
Relative Pitx2 expression
h
**
Relative Plod2 expression
i
**
Relative Col1a1 expression
Pitx2-GFP + + + + + + + +
mCherry MMP14 - + - + - + - +

Figure 8

a

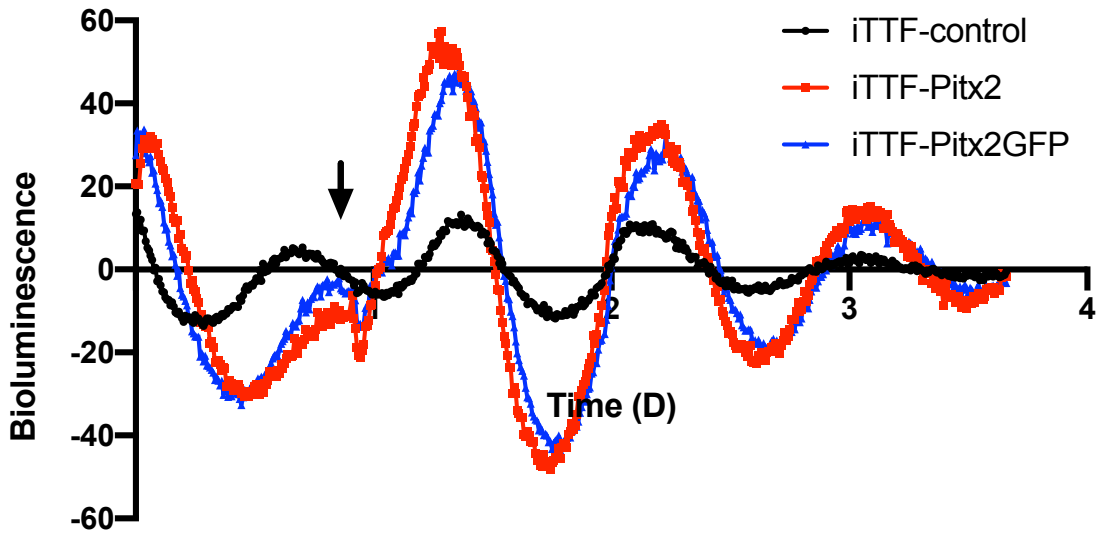
60
40
20
0
-20
-40
-60
Bioluminescence
2
3
4
Time (D)
iTTF-control
iTTF-Pitx2
iTTF-Pitx2GFP

b

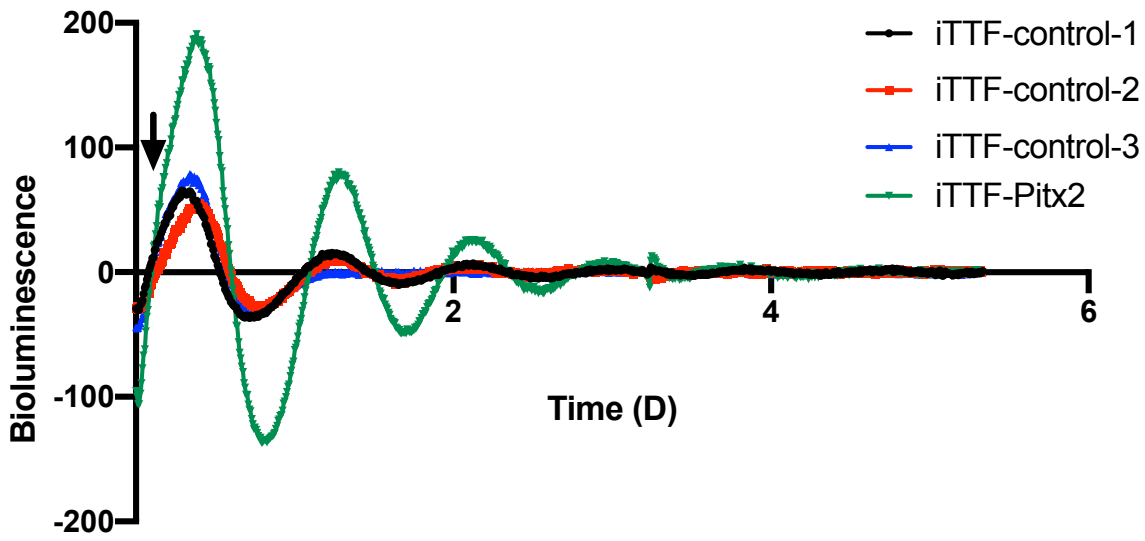
200
100
0
-100
-200
Bioluminescence
2
4
6
Time (D)
iTTF-control-1
iTTF-control-2
iTTF-control-3
iTTF-Pitx2

Extended data figure 1

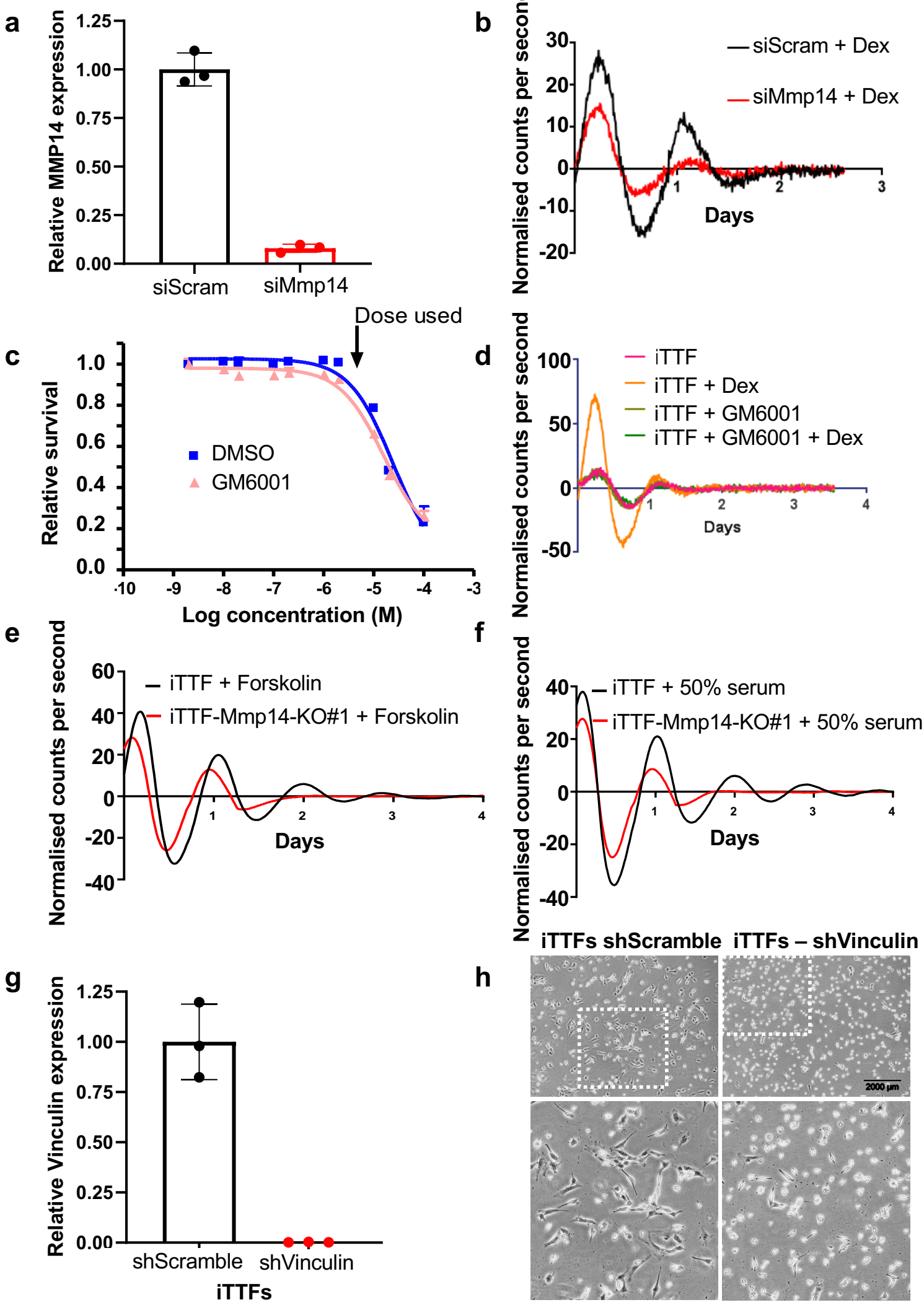

Extended data figure 2

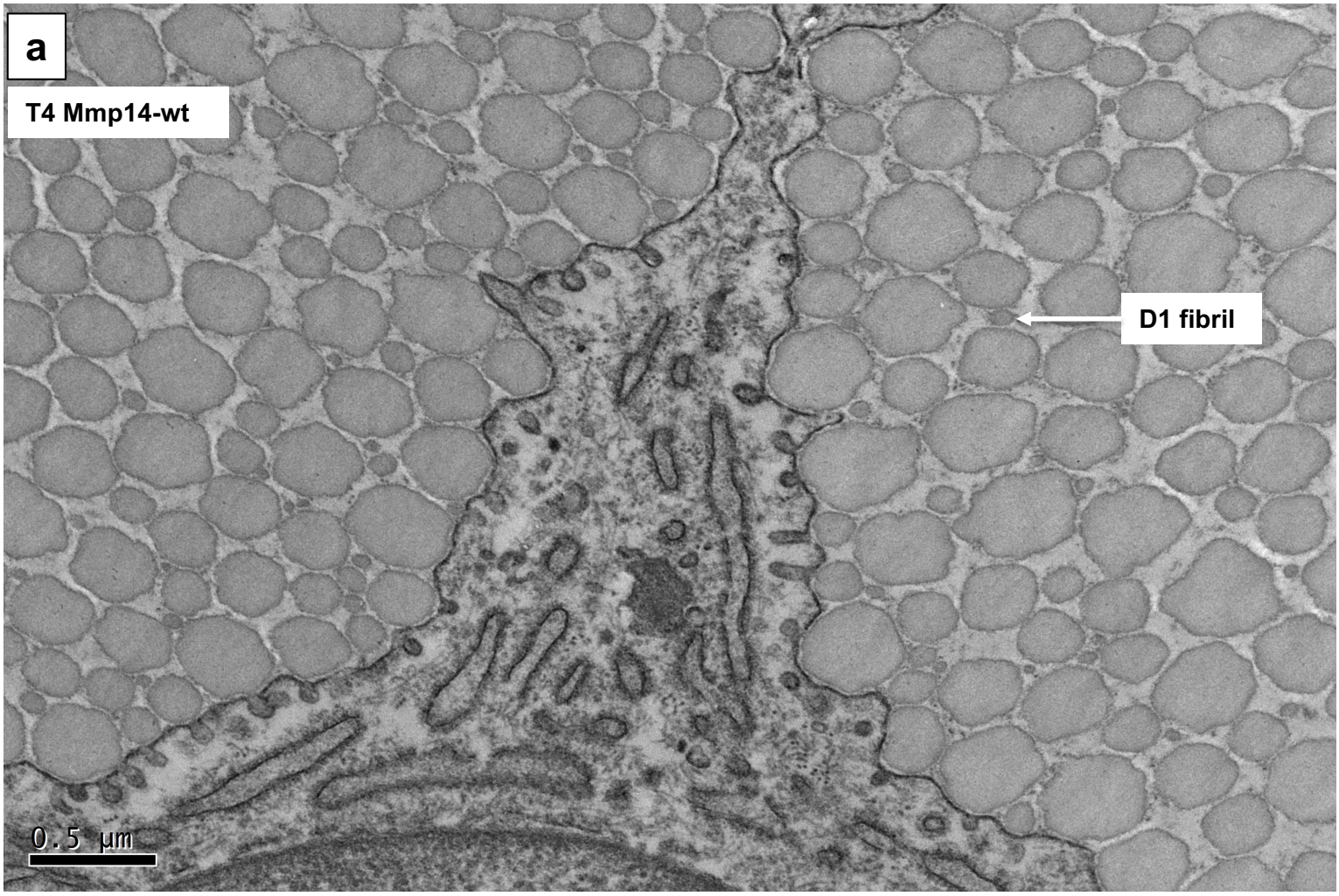

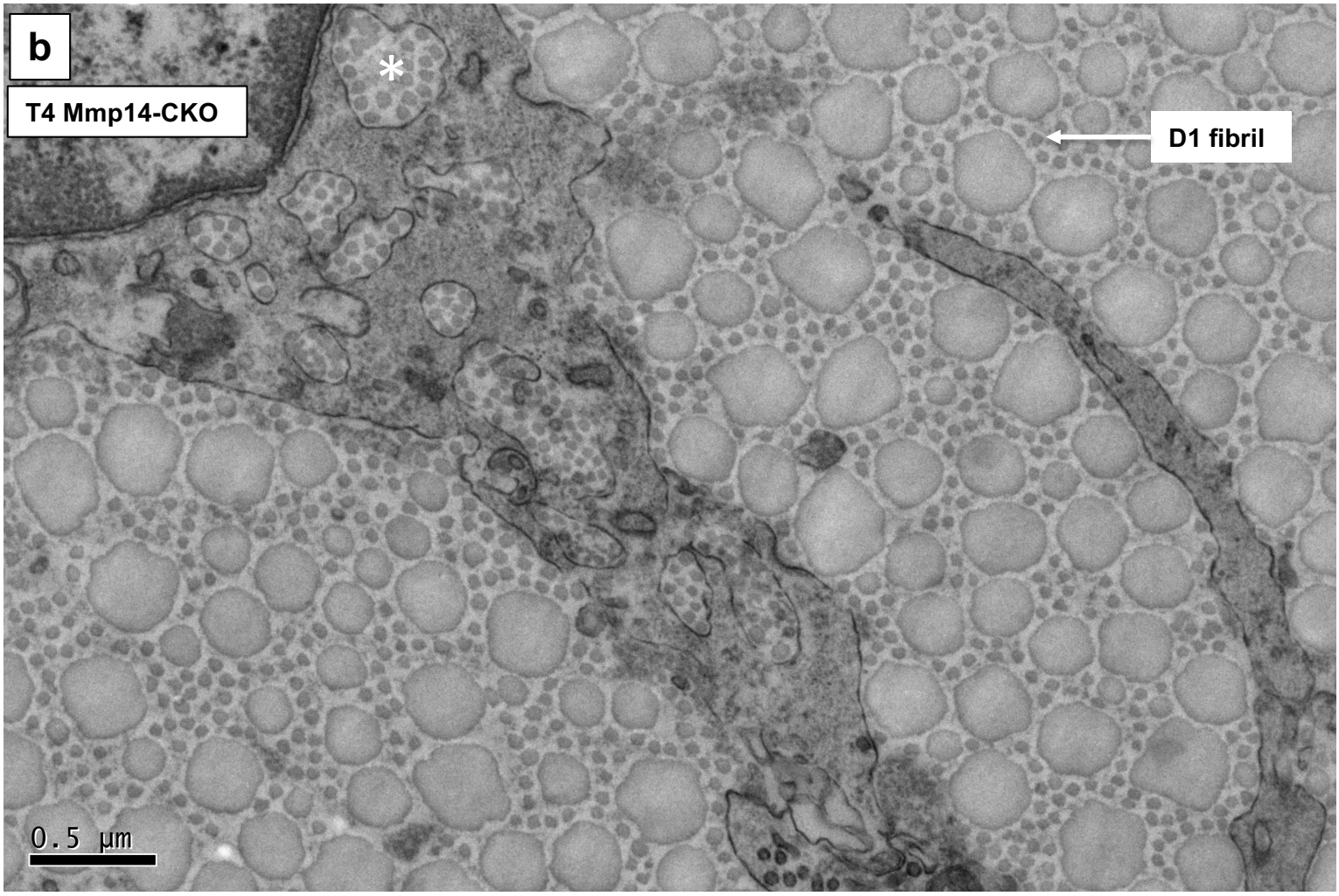

Extended data figure 3

a

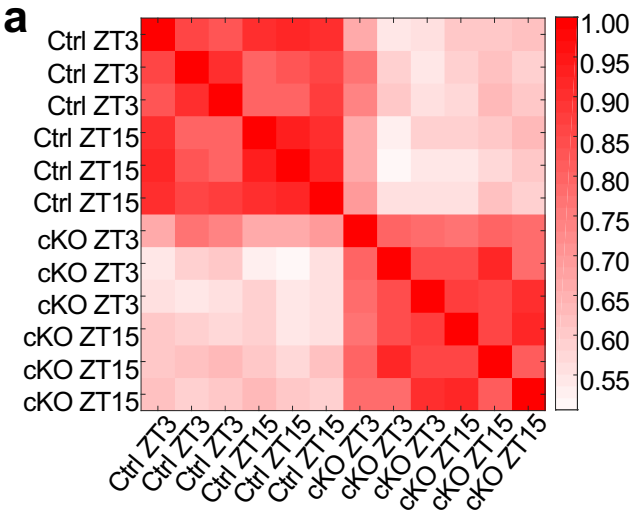

b

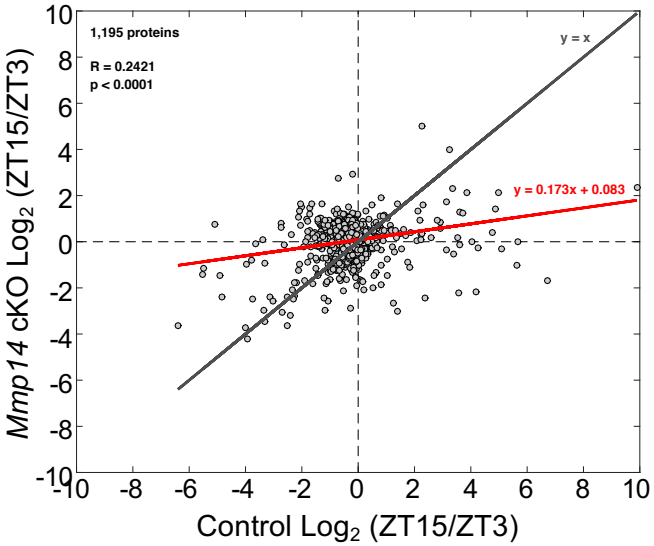

Extended data figure 4

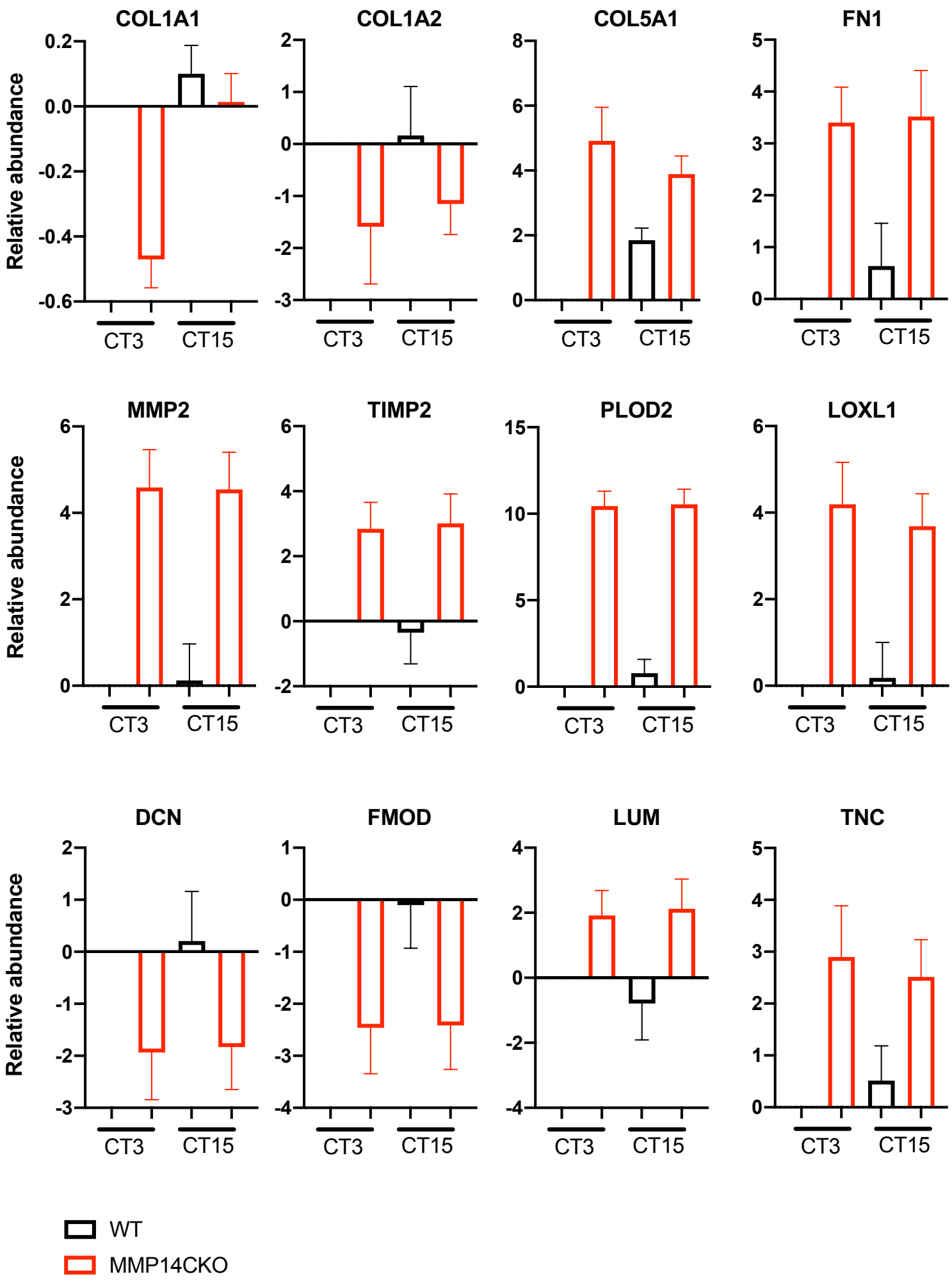

Unprocessed blots for Figure 1

WT mouse tail tendons: CT 3 7 11 15 19 23

Control lysates: *Scx-Cre::Mmp14*$^{fl/fl}$: b m t

b, bone
m, muscle
t, tendon

WB: MT1-MMP

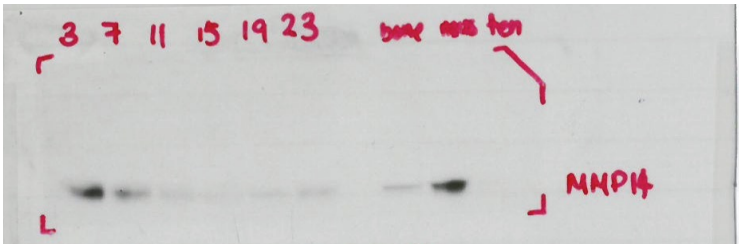

WB: GAPDH

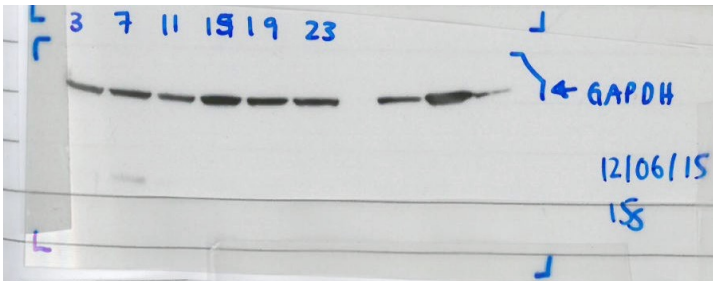
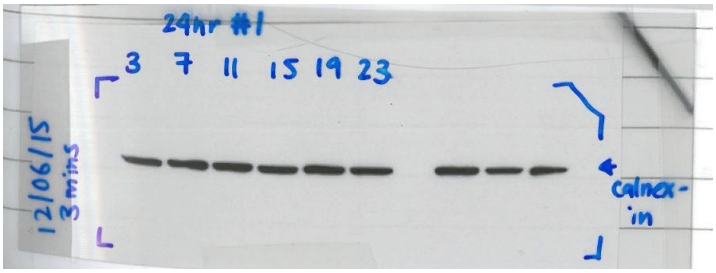
WB: Calnexin